

Tuning Frictional Properties of Kirigami Altered Graphene Sheets using Molecular Dynamics and Machine Learning

Designing a Negative Friction Coefficient

Mikkel Metzsch Jensen



Thesis submitted for the degree of
Master in Computational Science: Materials Science
60 credits

Department of Physics
Faculty of mathematics and natural sciences

UNIVERSITY OF OSLO

Spring 2023

Tuning Frictional Properties of Kirigami Altered Graphene Sheets using Molecular Dynamics and Machine Learning

Designing a Negative Friction Coefficient

Mikkel Metzsch Jensen



© 2023 Mikkel Metzsch Jensen

Tuning Frictional Properties of Kirigami Altered Graphene Sheets using Molecular Dynamics and Machine Learning

<http://www.duo.uio.no/>

Printed: Reprocentralen, University of Oslo

Abstract

Abstract.

Acknowledgments

Acknowledgments.

List of Symbols

F_N Normal force (normal load)

Acronyms

CM Center of Mass. 11, 30, 31

FFM Friction Force Microscopes. 9

MD Molecular Dynamics. 2, 3, 9, 25, 26, 29

ML Machine Learning. 2, 3, 26

NN Nearest neighbours. 13

SFA Surface force apparatus. 9

std Standard Deviation. 32, 33

Contents

1	Introduction	1
1.1	Motivation	1
1.2	Goals	3
1.3	Contributions	3
1.4	Thesis structure	3
I	Background Theory	5
II	Simulations	7
2	Defining the system	9
2.1	Region definitions	9
2.2	Numerical procedure	11
2.3	Creating the substrate	12
2.4	Creating the sheet	12
2.4.1	Indexing	13
2.4.2	Removing atoms	14
2.5	Kirigami patterns	15
2.5.1	Tetrahedron	16
2.5.2	Honeycomb	17
2.5.3	Random walk	18
2.5.3.1	Fundamentals	19
2.5.3.2	Spacing of walking paths	20
2.5.3.3	Bias	20
2.5.3.4	Stay or break	21
2.5.3.5	Deployment schemes	22
2.5.3.6	Validity	23
2.5.3.7	Random walk examples	24
3	Pilot study	25
3.1	Friction simulation parameters	25
3.2	Force traces	26
3.2.1	Force oscillations	26
3.2.2	Decompositions	30
3.2.3	Center of mass path	30
3.3	Defining metrics for friction	32
3.3.1	Kinetic friction	32
3.3.2	Static friction	33
3.4	Out-of-plane buckling	34
3.5	Investigating selected parameters	36
3.6	Normal force and stretch dependencies	38
3.6.1	Pressure reference for normal load domain	39

3.6.2 Contact area	39
3.6.3 Stretch	40
3.6.4 Normal force	42
3.7 Computational cost	43
Appendices	45
Appendix A	47
Appendix B	49
Appendix C	51

Chapter 1

Introduction

Structure of Motivation section:

1. Introduce and motivate friction broadly.
2. Motives for friction control using a grasping robot as example.
3. Analog to gecko feet where adhesive properties are turned on and off.
4. Interest in origin of friction through nanoscale studies which further motivates the use of MD.
5. Intro to metamaterials and the use of kirigami designs,
6. How to optimize kirigami designs with reference to Hanakata and motivating the use of ML.
7. Out-of-plane buckling motivates the use of kirigami for frictional properties.

Does some of the latter paragraphs belong to the approach section?

1.1 Motivation

Friction is a fundamental force that takes part in most of all interactions with physical matter. Even though the everyday person might not be familiar with the term *friction* we recognize it as the inherent resistance to sliding motion. Some surfaces appear slippery and some rough, and we know intuitively that sliding down a snow covered hill is much more exciting than its grassy counterpart. Without friction, it would not be possible to walk across a flat surface, lean against the wall without falling over or secure an object by the use of nails or screws [p. 5] [1]. It is probably safe to say that the concept of friction is integrated in our everyday life to such an extent that most people take it for granted. However, the efforts to control friction dates back to the early civilization (3500 B.C.) with the use of the wheel and lubricants to reduce friction in translational motion [2]. Today, friction is considered a part of the wider field *tribology* derived from the Greek word *Tribos* meaning “rubbing” and includes the science of friction, wear and lubrication [2]. The most compelling motivation to study tribology is ultimately to gain full control of friction and wear for various technical applications. Especially, reducing friction is of great interest as this has tremendous advantages for energy efficiency. It has been reported that tribological problems have a significant potential for economic and environmental improvements [3]:

“On global scale, these savings would amount to 1.4% of the GDP annually and 8.7% of the total energy consumption in the long term.” [4].

On the other hand, the reduction of friction is not the only sensible application for tribological studies. Controlling frictional properties, besides minimization, might be of interest in the development of a grasping robot where a finetuned object handling is required. While achieving a certain “constant” friction response is readily obtained through appropriate material choices during manufacturing, we are yet to unlock the capabilities to alter friction dynamically on the go. One example from nature inspiring us to think along these lines are the gecko feet. More precisely, the Tokay gecko has received a lot of attention in scientific studies aiming to unravel the underlying

mechanism of its “toggable” adhesion properties. Although geckos are able to produce large adhesive forces, they retain the ability to remove their feet from an attachment surface at will [5]. This makes the gecko able to achieve a high adhesion on the feet when climbing a vertical surface while lifting it for the next step remains relatively effortless. For a grasping robot we might consider an analog frictional concept of a surface material that can change from slippery to rough on demand depending on specific tasks.

In the recent years an increasing amount of interest has gone into the studies of the microscopic origin of friction, due to the increased possibilities in surface preparation and the development of nanoscale experimental methods. Nano-friction is also of great concern for the field of nano-machining where the frictional properties between the tool and the workpiece dictates machining characteristics [3]. With concurrent progress in computational power and development of Molecular Dynamics (MD), numerical investigations serve as an extremely useful tool for getting insight into the nanoscale mechanics associated with friction. This simulation based approach can be considered as a “numerical experiment” enabling us to create and probe a variety of high complexity systems which are still out of reach for modern experimental methods.

In materials science such MD-based numerical studies have been used to explore the concept of so-called *metamaterials* where material compositions are designed meticulously to enhance certain physical properties [6][7][8][9][10][11]. This is often achieved either by intertwining different material types or removing certain regions completely. In recent papers by Hanakata et al. [6](2018) [7](2020) numerical studies have showcased that mechanical properties of a graphene sheet, in this case yield stress and yield strain, can be altered through the introduction of so-called *kirigami* inspired cuts into the sheet. Kirigami is a variation of origami where the paper is cut additionally to being folded. While these methods originate as an art form, aiming to produce various artistic objects, they have proven to be applicable in a wide range of fields such as optics, physics, biology, chemistry and engineering [12]. Various forms of stimuli enable direct 2D to 3D transformations through folding, bending, and twisting of microstructures. While original human designs have contributed to specific scientific applications in the past, the future of this field is highly driven by the question of how to generate new designs optimized for certain physical properties. However, the complexity of such systems and the associated design space makes for seemingly intractable problems ruling out analytic solutions.

Earlier architecture design approaches such as bioinspiration, looking at gecko feet for instance, and Edisonian, based on trial and error, generally rely on prior knowledge and an experienced designer [9]. While the Edisonian approach is certainly more feasible through numerical studies than real world experiments, the number of combinations in the design space rather quickly becomes too large for a systematic search, even when considering the simulation time on modern day hardware. However, this computational time constraint can be relaxed by the use of machine learning (ML) which have proven successful in the establishment of a mapping from the design space to physical properties of interest. This gives rise to two new styles of design approaches: One, by utilizing the prediction from a trained network we can skip the MD simulations all together resulting in an *accelerated search* of designs. This can be further improved by guiding the search accordingly to the most promising candidates, as for instance done with the *genetic algorithm* which suggest new designs based on mutation and crossing of the best candidates so far. Another, even more sophisticated approach, is through generative methods such as *Generative Adversarial Networks* (GAN). By working with a so-called *encoder-decoder* network structure, one can build a model that reverses the prediction process. That is, the model predicts a design from a set of physical target properties. In the papers by Hanakata et al. both the *accelerated search* and the *inverse design* approach was proven successful to create novel metamaterial kirigami designs with the graphene sheet.

Hanakata et al. attributes the variety in yield properties to the non-linear effects arising from the out-of-plane buckling of the sheet. Since it is generally accepted that the surface roughness is of great importance for frictional properties it can be hypothesized that the kirigami cut and stretch procedure can also be exploited for the design of frictional metamaterials. For certain designs we might hope to find a relationship between stretching of the sheet and frictional properties. If significant, this could give rise to a variability of the friction response beyond manufacturing material choice. For instance, the grasping robot might apply such a material as artificial skin for which stretching or relaxing of the surface could result in a changeable friction strength; Slippery and smooth when in contact with people and rough and firmly gripping when moving heavy objects. In addition, a possible coupling between stretch and the normal load through a nanomachine design would allow for an altered friction coefficient. This invites the idea of non-linear friction coefficients which might in theory also take on negative values given the right response from stretching. The latter would constitute an extremely rare property. This has (**only?**) been reported indirectly for bulk graphite by Deng et al. [13] where the friction kept increasing during the unloading phase. **Check for other cases and what I can really say here.**

To the best of our knowledge, kirigami has not yet been implemented to alter the frictional properties of a nanoscale system. In a recent paper by Liefferink et al. [14](2021) it is reported that macroscale kirigami can be used to dynamically control the macroscale roughness of a surface through stretching which was used to change the frictional coefficient by more than one order of magnitude. This supports the idea that kirigami designs can in fact be used to alter friction, but we believe that taking this concept to the nanoscale regime would involve a different set of underlying mechanisms and thus contribute to new insight in this field.

1.2 Goals

In this thesis we investigate the possibility to alter and control the frictional properties of a graphene sheet through application of kirigami inspired cuts and stretching of the sheet. With the use of MD simulations we evaluate the friction properties under different physical conditions in order to get insight into the prospects of this field. By evaluating variations of two kirigami inspired patterns and a series of random walk generated patterns we create a dataset containing information of the frictional properties associated with each design under different load and stretch conditions. We apply ML to the dataset and use an accelerated search approach to optimize for different properties of interest. The subtask of the thesis are presented more comprehensively in the following.

1. Define a sheet indexing that allows for a unique mapping of patterns between a hexagonal graphene lattice representation to a matrix representation suited for numerical analysis.
2. Design a MD simulation procedure to evaluate the frictional properties of a given graphene sheet under specified physical conditions such as load, stretch, temperature etc.
3. Find and implement suitable kirigami patterns which exhibit out-of-plane buckling under tensile load. This includes the creation of a framework for creating variations within each pattern class. Additionally create a procedure for generating different styles of random walk patterns.
4. Perform a pilot study of a representative subset of patterns in order to determine appropriate simulation parameters to use for the further study along with an analysis of the frictional properties shown in the subset.
5. Create a dataset consisting of the chosen kirigami variations and random walk patterns and analyse data trends.
6. Train a neural network to map from the design space to physical properties such as mean friction, maximum friction, contact area etc. and evaluate the performance.
7. Perform an accelerated search optimizing for interesting frictional properties using the ML model. This should be done both through the pattern generation procedures and by following a genetic algorithm approach.
8. Use the most promising candidates from the accelerated search to investigate the prospects of creating a nanomachine setup which exhibits a negative friction coefficient.
9. Study certain designs of interest with the scope of revealing underlying mechanism. This includes simple correlation analysis but also a visualization of feature and gradient maps of the ML network.

Is the list of subtask too specific? Some of the details here might be better suited for the thesis structure section.

1.3 Contributions

What did I actually achieve

1.4 Thesis structure

How is the thesis structured.

Part I

Background Theory

Part II

Simulations

Chapter 2

Defining the system

The definition of the system plays an essential role as it sets the scene for the whole study. With the general goal of investigating the frictional behaviour of a graphene sheet, as we alter it through kirigami cuts and stretch, two different approaches were considered as sketched in Fig. 2.1. One approach is simply to mimic a FFM type experiment as done in most other numerical friction studies. In this case, we probe the graphene sheet, resting on a substrate, with an indenting tip connected to a moving body. Friction is then measured by making the tip scan across the graphene surface. This setup allows for a variety of tip shapes and sizes, and alternatively the tip can be substituted with a flat surface making the setup resemble a SFA experiment. It is not obvious how one would achieve the stretching of the sheet, but a simple solution is to pre-stretch the sheet to a given amount and then fixating it, by the ends, on the substrate. We are then able to investigate the frictional behaviour at different amounts of stretching between simulations. If any interesting behaviour is found, at a certain stretch amount, a possible application would call for the attachment of a pre-stretched sheet as a surface coating. Another option is to attach the graphene sheet to the moving body instead and introduce some sort of nanomachine in the moving body coupling the normal load with a stretching motion. This gives more design room to utilize any stretch-related friction effects that require a dynamical changing of the stretch amount throughout the loading. While both methods serve as novel approaches with prospects of providing valuable insight into a sparsely covered field, we choose the latter option due to the increased application design freedom. Hence, our system of choice consists of two separate parts: A 2D graphene sheet and a 3D Silicon “bulk” substrate. Note, that we do attempt to model the nanomachine explicitly in this study, but we will consider the prospects of adding this in ??.

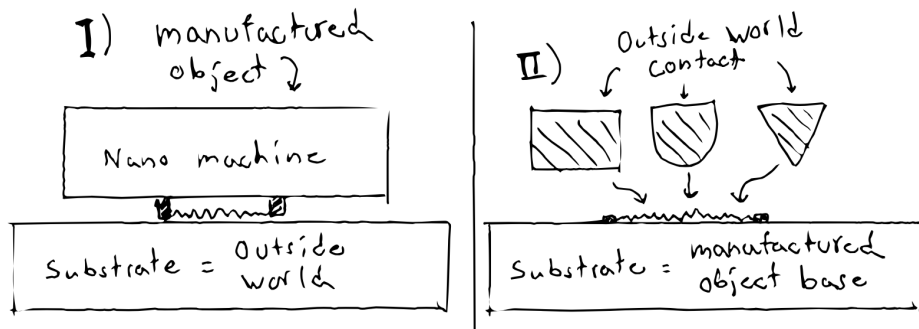


Figure 2.1: TMP System variations

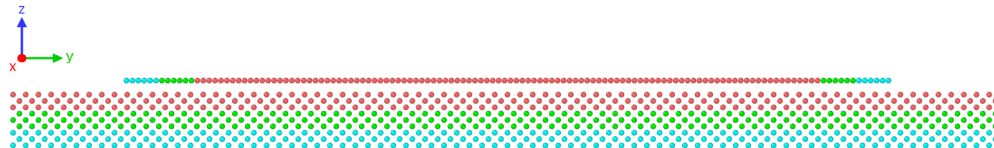
2.1 Region definitions

We subdivide the two main parts of the simulation, the sheet and the substrate, into specific regions according to their functionality in the MD simulations. For the sheet, we denote a subsection of the ends, with respect to the sliding direction, as so-called *pull blocks*, which is reserved for the application of normal load, stretching and dragging of the sheet, and for applying the thermostat. The remaining *inner sheet* is left for the kirigami cuts and are simulated as an *NVE* ensemble. The pull blocks are equally split between a thermostat part and a

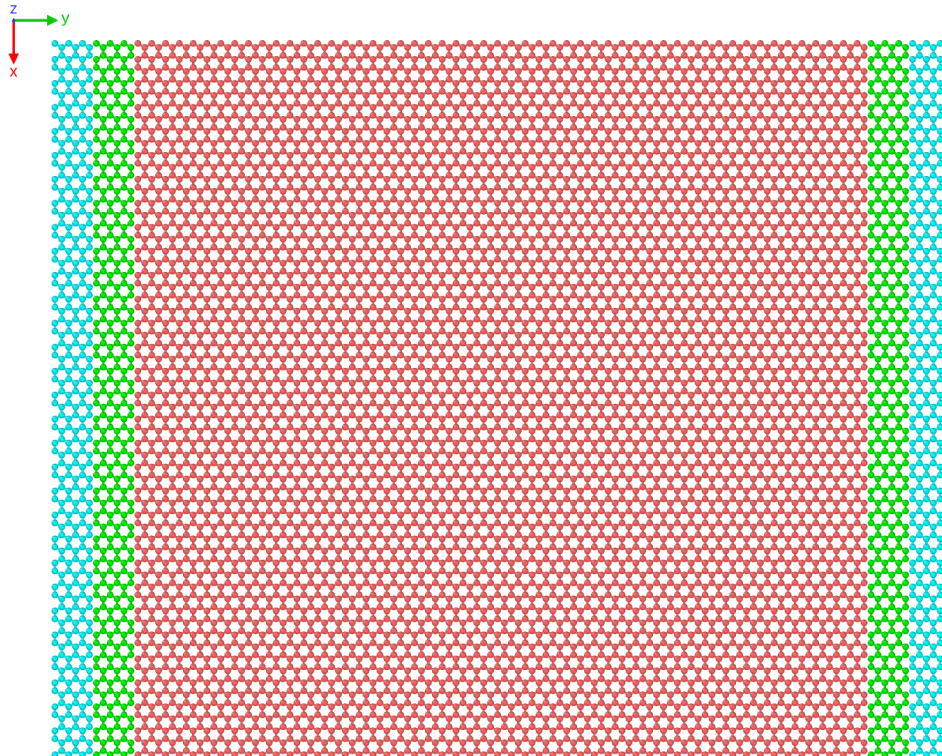
rigid part. The rigid part is however thermolized during the initial relaxation period but made rigid for the final duration of the simulation. Note that the rigid parts on both sides of the sheet is then considered as a single rigid object even though they are physically separated. This means that all force interactions concerning the rigid parts will be applied as a common average making them move in total synchronization. The substrate is equally divided into three parts: The *upper layers* (*NVE*) responsible for the sheet-substrate interaction, the *middle layers* being a thermostat (*NVT*), and the *bottom layers* being frozen, made rigid and fixed, in the initial lattice structure to ensure that the substrate stays in place. In Fig. 2.2 the system is displayed with colors matching the three distinct roles:

1. Red: *NVE* parts which is governing the frictional behaviour of interest.
2. Green: Thermostats (*NVT*) surrounding the *NVE* parts in order to modify the temperature without making disturbing changes to the interaction of the sheet and substrate.
3. Blue: Parts that are initially or eventually turned in to rigid objects. For the substrate this refers to an additionally fixation as well.

The full sheet is given a size $\sim 130 \times 163 \text{ \AA}$ while the substrate is scaled accordingly to the sheet which is further specified in Sec. 2.3. For an expected stretch of 200% the total system size is roughly 55k atoms. The specific distribution is shown in Table 2.2 along with the spatial x-y-measures in Table 2.1.



(a) Side view showing sheet on top of the substrate.



(b) Top view showing only the sheet.

Figure 2.2: System configuration colorized to indicate *NVE* parts (red), thermostat parts (green) and rigid parts (blue).

Table 2.1: Specification of the spatial size of the system for the x-y-dimensions with a substrate scaled for an expected stretch of 200%. The first column denotes the size relative to the full sheet size $x_S \times y_S$, while the second column denotes the corresponding length in Å.

Region	Dim	Dim [Å]	Area [Å ²]
Full sheet	$x_S \times y_S$	130.029 × 163.219 Å	21,223.203
Inner sheet	$x_S \times 0.81 y_S$	130.029 × 132.853 Å	17,274.743
Pull blocks	$2 \times x_S \times 0.09 y_S$	$2 \times 130.029 \times 15.183$ Å	$2 \times 1,974.230$
Substrate	$1.16 x_S \times 3.12 y_S$	150.709 × 509.152 Å	76,733.789

Table 2.2: Specification of the system size in number of atoms for various system regions. These numbers corresponds with the case of no cuts applied to the sheet and a substrate scaled for the expected stretch of 200 %.

Region	Total	Sub region	Sub total	NVE	NVT	Rigid
Full sheet	7800	Inner sheet	6360	6360	0	0
		Pull blocks	1440	0	720	720
Substrate	47376	Upper	15792	15792	0	0
		Middle	15792	0	15792	0
		Bottom	15792	0	0	15792
All	55176			22152	16512	16512

2.2 Numerical procedure

The numerical procedure related to the measurement of friction can be arranged into the following steps. Some steps have been given a default duration denoted in parentheses in units of ps, 10^{-12} seconds.

- 1. Relaxation** (15 ps): The sheet and substrate are relaxed for 15 ps after being added in their crystalline form with a separation distance of 3 Å. The equilibrium separation distance varies slightly with temperature, but we found this number to be a reasonable middle ground for the temperature range of interest. The sheet is constrained under three hard spring forces, all with spring constant 10^5 eV/Å² $\sim 1.6 \times 10^6$ N/m: One spring attaches the sheet center of mass (CM) to its original position, preventing any drift. The remaining two springs are attached to the pull block ends, to their initial CM position respectively, to prevent rotation. In principle, it would be sufficient to fixate just one of the ends in order to stop rotation, but we fixate both ends for the sake of symmetry. During the relaxation phase the pull blocks are made rigid with respect to the z-direction only (perpendicular to the sheet). That is, all the forces in the z-direction are summed up and distributed on the pull blocks as a single external force, while it is free to expand and contract in the x-y-plane. This is mainly to ensure that it achieves the correct lattice spacing according to the temperature of the system. For the following phases the rigid parts of the pull block is in fact rigid with respect to all directions. The spring forces are terminated after the relaxation phase.
- 2. Stretch:** The sheet is stretched by separating the two opposing rigid parts of the pullblock at constant velocity until the desired stretch amount is met. The duration of this phase is thus governed by the *stretch speed* and *stretch amount* parameters.
- 3. Pause** (5 ps): The sheet is relaxed for 5 ps to ensure that the sheet is stable and equilibrated after the applied stretch deformation.
- 4. Normal load** (5 ps): The normal load is applied to the rigid parts of the pull blocks. Initially a viscous damping force, $F = -\gamma v$, is added to the sheet to resist the rapid acceleration of the sheet and prevent a hard impact between the sheet and substrate. The damping coefficient is set to $\gamma = 8 \times 10^{-4}$ nN/(m/s) and terminated after 0.5 ps which was found to be suitable for the extreme load cases of our intended range. The remaining 4.5 ps is simply devoted for further relaxation.

5. **Sliding:** A virtual atom is introduced into the simulation which exclusively interacts with the rigid parts of the pull blocks through a spring force with variable spring constant K in the x-y-plane. The z-direction is not affected by the spring force and is purely governed by the balancing forces of the normal load and the normal response from the sheet-substrate interaction. The virtual atom is immediately given a constant velocity, in accordance to the *sliding speed* parameter, which make the sliding force increase quadratically, $F_{slide} \propto K(v_{slide})^2$, with sliding speed. An infinite spring constant can also be enforced for which the spring is omitted and the pull blocks are moved rigidly with a constant speed according to the sliding speed.

In order to prevent rupturing, or detachment, of the sheet, we monitor the nearest neighbours for each atom throughout the simulation. At the initial timestep the three nearest neighbours, sitting at a distance 1.42 Å, of all graphene atoms is recorded. If any of these nearest neighbours exceeds a threshold distance of 4 Å, indicating a bond breakage, this is marked as a rupture and we halt the simulation early. Thus, we ensure that no wear is taking place for the sheet. The substrate was proven to be way more resistant to wear, and by running a few test simulations of high load and sliding speed we confirmed visually that no wear is occurring.

2.3 Creating the substrate

The substrate is created as a rectangular slab of Silicon (Si). We create the initial configuration according to its crystalline structure given as a diamond cubic crystal with a lattice parameter $a_{Si} = 5.43$ Å. The default substrate thickness is chosen such that 9 layers of atoms appear (2 unit cells) corresponding to a thickness of 10.86 Å. The x-y dimensions are chosen to match the dimensions. That is, we define a margin between the sheet edge and the substrate edge for the x- and y-direction respectively. Since we use periodic boundary conditions a too small margin would result in the sheet edges interacting with themselves through the boundary. The absolute lower limit for the margin choice is thus half the cut-off distance for the Tersoff potential, governing the graphene sheet interaction, at $R + D = 2.1$ Å. However, due to fluctuations in the sheet we cannot set the margin to close to that limit. Additionally, we must take into account the buckling of the sheet as it is stretched, which might induce an expansion in the x-direction for certain configurations. We choose a x-margin of 20 Å which provides $2 \cdot 20$ Å – 2.1 Å = 37.9 Å of additional spacing with respect to the absolute lower limit. By looking over the simulation result visually we confirm that this leaves more than enough room in the cases of extreme buckling. For the y-direction the rigid parts of the pull-blocks move a certain distance based on the stretch value exclusively, and we define the y-margin based on the remaining distance to the edge after stretching. However, as the sheet travels through the periodic boundaries in the y-direction when sliding, we want to add some additional spacing through the y-margin in order to let the substrate surface relax before interacting with the sheet a second time. We choose a y-margin of 15 Å for which the preferred sliding speed of 20 m/s = 2 Å/ps gives 15 ps of relaxation time between encounters with the sheet, similar to the initial relaxation time.

2.4 Creating the sheet

The sheet is created by the 2D material known as graphene which consist of a single layer of carbon atom arranged in hexagonal lattice structure. The bulk version of this material is called graphite and simple refers to the merged structure of multiple graphene layers. We can describe the 2D crystal structure in terms of its primitive lattice vectors \mathbf{a}_1 and \mathbf{a}_2 and a basis. The basis describes the .. part of the crystal and we populate each lattice site by the given basis and translate it to fill the whole plane by any linear combination of the lattice vectors

$$\mathbf{T}_{mn} = m\mathbf{a}_1 + n\mathbf{a}_2, \quad m, n \in \mathbb{N}.$$

For graphene, we have the primitive lattice vectors

$$\mathbf{a}_1 = a \left(\frac{\sqrt{3}}{2}, -\frac{1}{2} \right), \quad \mathbf{a}_2 = a \left(\frac{\sqrt{3}}{2}, \frac{1}{2} \right), \quad |\mathbf{a}_1| = |\mathbf{a}_2| = 2.46 \text{ Å}.$$

Notice that we deliberately excluded the third coordinate as we only consider a single graphene and thus we do not have to consider the stacking structure of 3D graphite. The basis consist of two carbon atoms given as

$$\left\{ (0,0), \frac{a}{2} \left(\frac{1}{\sqrt{3}}, 1 \right) \right\}$$

The crystal structure is visualized in Fig. 2.3. It turns out that the spacing between atoms is equal for all pairs of atoms with an interatomic distance

$$\left\| \frac{a}{2} \left(\frac{1}{\sqrt{3}}, 1 \right) \right\| \approx 1.42 \text{ \AA}.$$

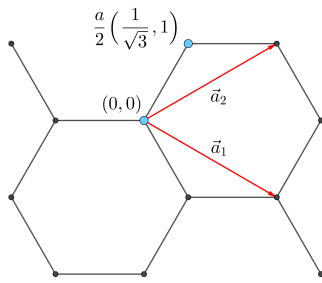


Figure 2.3: Graphene crystal structure with basis.

2.4.1 Indexing

In order to define the cut patterns applied to the graphene sheet we need to define an indexing system. We must ensure that this gives an unique description of the atoms as we eventually want to pass a binary matrix, containing 0 for removed atoms and 1 for present atoms, that uniquely describes the sheet. We do this by letting the x-coordinate align with the so-called *armchair* direction of the sheet and making the y-coordinate increment along the so-called *zigzag* direction. Notice that the x-coordinate will point to *zigzag* chains of atoms for which the starting point, at $y = 0$ is not evenly spaced as illustrated in figure Fig. 2.4. Other solutions might naturally involve the lattice vectors, but since these are used to translate between similar basis atoms it introduces an unfortunate duality as one would then need to include the basis atom of choice into the indexing system as well. Additionally, we want an indexing system which conserves the relative physical position of neighbours. That is, atom (i, j) should be in the proximity of $\{(i+1, j), (i-1, j), (i, j+1), (i, j-1)\}$. However, due to the hexagonal structure of the lattice, only three said neighbour indexes will be actual nearest neighbours in the lattice. While $(i, j \pm 1)$ is always a nearest neighbour, the index of the nearest neighbour in the x-direction oscillate for each incrementing of x- or y-coordinate. That is, the nearest neighbours (NN) is decided as

$$(i+j) \text{ is even} \rightarrow \text{NN} = \{(i-1, j), (i, j+1), (i, j-1)\}, \\ (i+j) \text{ is odd} \rightarrow \text{NN} = \{(i+1, j), (i, j+1), (i, j-1)\}. \quad (2.1)$$

By consulting Fig. 2.4 we can verify this visually, and it basically comes down to the fact whether the atom is oriented to the right or the left side in the zigzag chain.

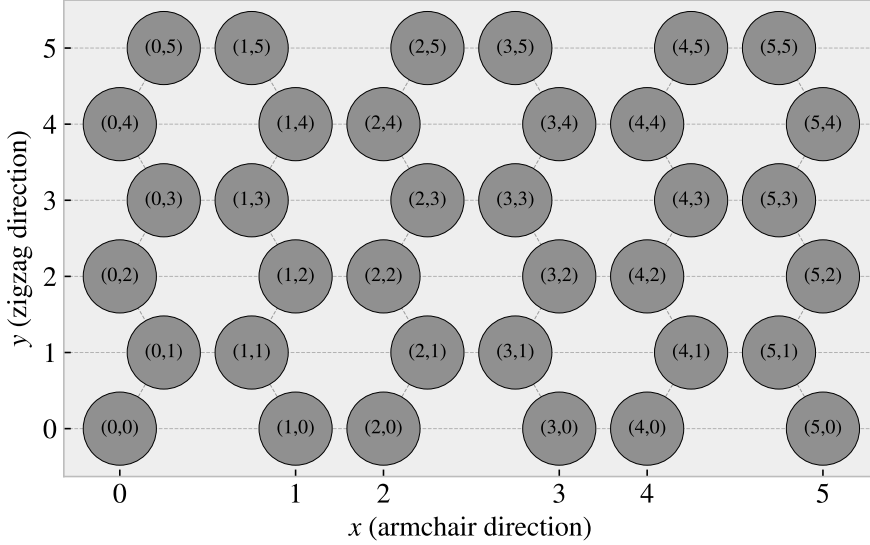


Figure 2.4: Graphene atom indexing

2.4.2 Removing atoms

As a means to ease the formulation of the cut patterns we introduce the *center element* placed in each gap of the hexagonal honeycomb structure as shown in figure Fig. 2.5. These are not populated by any atoms but will serve as a temporary reference for the algorithmic approaches of defining a cut pattern.

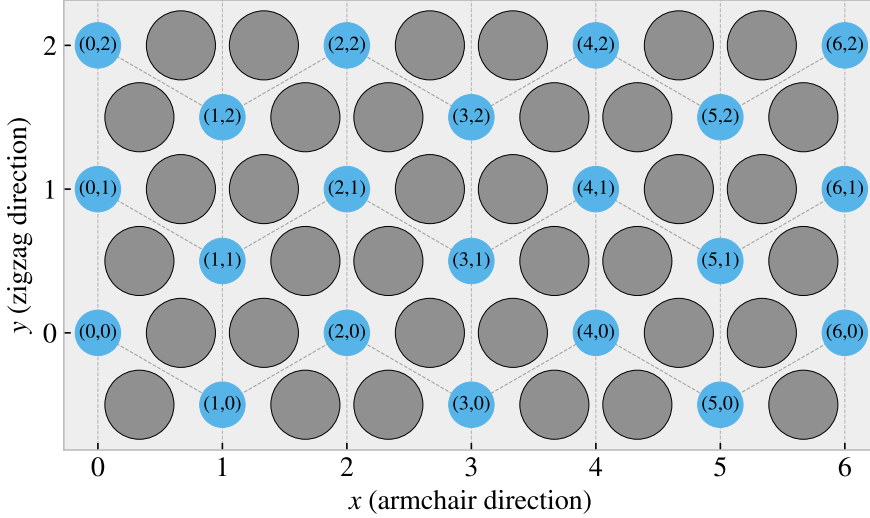


Figure 2.5: Graphene center indexing

Similar to the case of the atom indexing, the nearest neighbours center elements alternate with position, this time only along the x-coordinate index. Each center element has six nearest neighbours, in clockwise direction we can denote them: “up”, “upper right”, “lower right”, “down”, “lower left”, “upper left”. The “up” and “down” is always accessed as $(i, j \pm 1)$, but for even i the $(i + 1, j)$ index corresponds to the “lower right” neighbour while for odd i this corresponds to the “upper right” neighbour. This shifting applies for all left or right oriented neighbours and the full neighbour list is illustrated in Fig. 2.6.

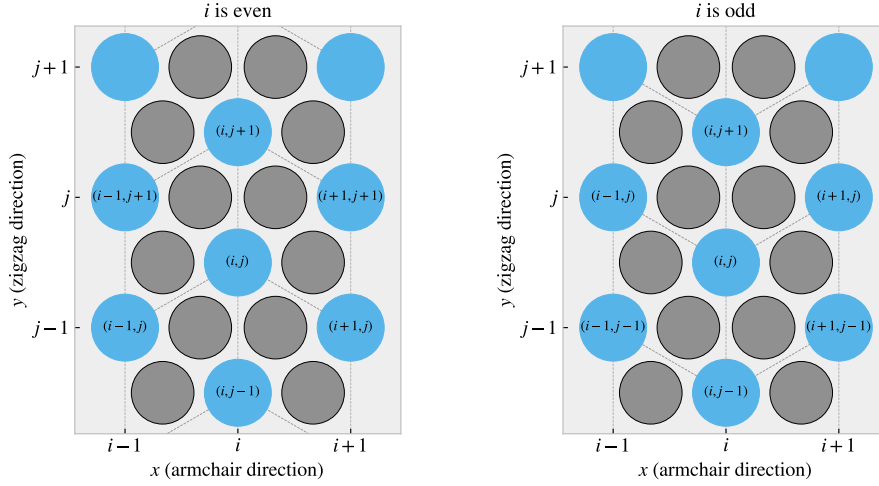


Figure 2.6: Graphene center elements directions

We define a cut pattern by connecting center elements into connected paths. As we walk from center element to center element we remove atoms according to one of two rules

1. Remove intersection atoms: We remove the pair of atoms placed directly in the path we are walking. That is, when jumping to the “up” center element we remove the two upper atoms located in the local hexagon of atoms. This method is sensitive to the order of the center elements in the path.
2. Remove all surrounding atoms: We simply remove all atoms in the local hexagon surrounding each center element. This method is independent of the ordering of center elements in the path.

We notice that removing atoms using either of these rules will not guarantee an injective, one to one, mapping. The first rule, being path dependent, will more often result in a unique result. However, for both methods it is possible to construct two different paths leading to the same cut pattern as shown in the following example:

$$\begin{aligned} \text{Path 1: } & (i, j) \rightarrow \underbrace{(i + 1, j + 1)}_{\text{upper right}} \rightarrow \underbrace{(i, j + 1)}_{\text{up}} \rightarrow \underbrace{(i + 1, j + 2)}_{\text{upper right + up}} \rightarrow \underbrace{(i + 1, j + 1)}_{\text{upper right}} \\ \text{Path 2: } & (i, j) \rightarrow \underbrace{(i + 1, j + 1)}_{\text{upper right}} \rightarrow \underbrace{(i + 1, j + 2)}_{\text{upper right + up}} \rightarrow \underbrace{(i, j + 1)}_{\text{up}} \end{aligned}$$

Illustrate the example path, because I think it is otherwise impossible to follow.

For the second rule it is even more obvious that different paths can result in the same final pattern. For instance, if we incircle a center element completely there will be no surrounding atoms left to delete when jumping to that center element. This highlights the importance of defining the atom based indexing system will yield an injective mapping for the binary cut matrix. However, using the center elements for reference makes the following definitions of the cut patterns a lot easier to design as we always can always go in the same six directions as opposed to the atom indexing system which have alternating directions for its neighbours.

2.5 Kirigami patterns

We propose a series of kirigami inspired cut patterns for the altering of the graphene sheet. We seek inspiration from macroscale patterns that showcases a considerable amount of out of plane buckling when stretched. We choose to imitate two different designs: 1) An alternating repeating series of perpendicular cuts as shown in Fig. 2.7a popularly used in studies of morphable metematerials [15]. This pattern produce surface buckling with a tetrahedron (three sided pyramid) shape when stretched. 2) A more intricate pattern shown in Fig. 2.7b which is used commercially by ScotchTM Cushion LockTM [16] as protective wrap for items during shipping. This pattern buckles into a hexagonal honeycomb structure when stretched. In addition to the modeling of the so-called *Tetrahedron* and *Honeycomb* patterns we also create a series of random walk cut patterns.



Figure 2.7: Macroscale kirigami cut patterns used as inspiration for the nanoscale implementation. (a) Tetrahedron: Alternating perpendicular cuts producing a tetrahedron shaped surface buckling when stretched [15]. (b) Honeycomb: ScotchTM Cushion LockTM [16] producing a honeycomb shaped surface buckling when stretched.

2.5.1 Tetrahedron

The *Tetrahedron* pattern is defined in terms of center elements for which all atoms surrounding a given center element are removed. The pattern is characterized by two straight cuts, denoted line 1 and line 2, arranged perpendicular to each other. This is done in such a way such that one line aligns with the center of the other line and with a given spacing in between. This is illustrated in Fig. 2.8. In order to achieve perpendicular cuts we cannot rely purely on the six principal directions corresponding to the center element neighbours which is spaced by 60° . We let line 1 run along the center elements in the direction of the “upper right” (and “lower left”) center elements while line 2 goes in the direction between the “down” and “lower right” (“up” and “upper left”) center elements, corresponding to the direction $(1/\sqrt{3}, -1)$. We define variations of the pattern by the number of center elements L_1 and L_2 in line 1 and 2 respectively, together with the spacing between the lines d , as the tuple (L_1, L_2, d) . The pattern is constructed by translating the two lines to the whole sheet according to the spacing. Due to the alignment criterias of having one line point to the center of the other line we can only have odd line length. Furthermore, in order to ensure that each center element is translated to an i -index of similar odd or eveness, we must in practice require that $|L_2 - L_1| = 2, 6, 10, \dots$. In Fig. 2.8 we see a visual representation of the pattern components for the $(7, 5, 2)$ pattern.

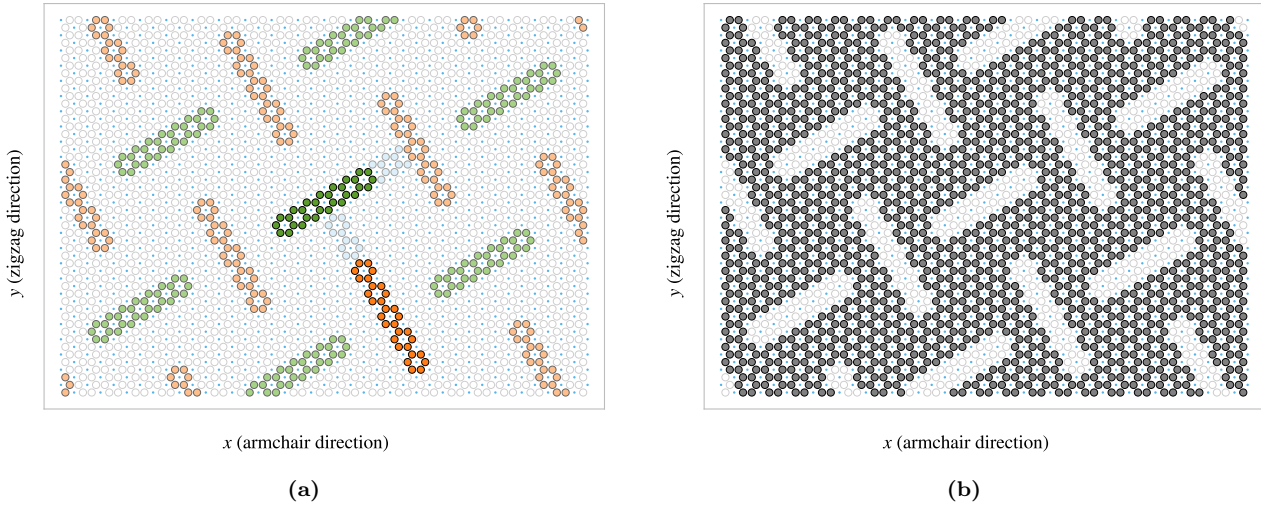


Figure 2.8: Visual representation of the tetrahedron pattern consisting of two perpendicular lines, line 1 and line 2, of length L_1 and L_2 respectively with spacing d . This example used $(L_1, L_2, d) = (7, 5, 2)$. (a) Highlight of the atoms removed. Line 1 is shown in green and line 2 in orange, with lighter colors for the translated variations, and the spacing is shown in light blue. (b) The sheet after applying the cut pattern where the grey circles denote atoms and the transparent white denotes removed atoms. The small blue circles show the center elements for reference. **Sheet size used in example**

In addition to the three parameters L_1, L_2, d , the pattern is also anchored to a reference point which describes the position of line 1 and 2 before translating to the whole sheet. Due to the repeating structure of the pattern there exist a small finite number of unique reference positions. For the pattern $(7, 5, 2)$ used as an example in Fig. 2.8, there are 140 ¹ unique reference points. Some additional variation of the pattern is showcased in Fig. 2.9 all with a reference position in the center of the sheet. Note that a smaller sheet size is used in both Fig. 2.8 and Fig. 2.9 for illustrative purposes.

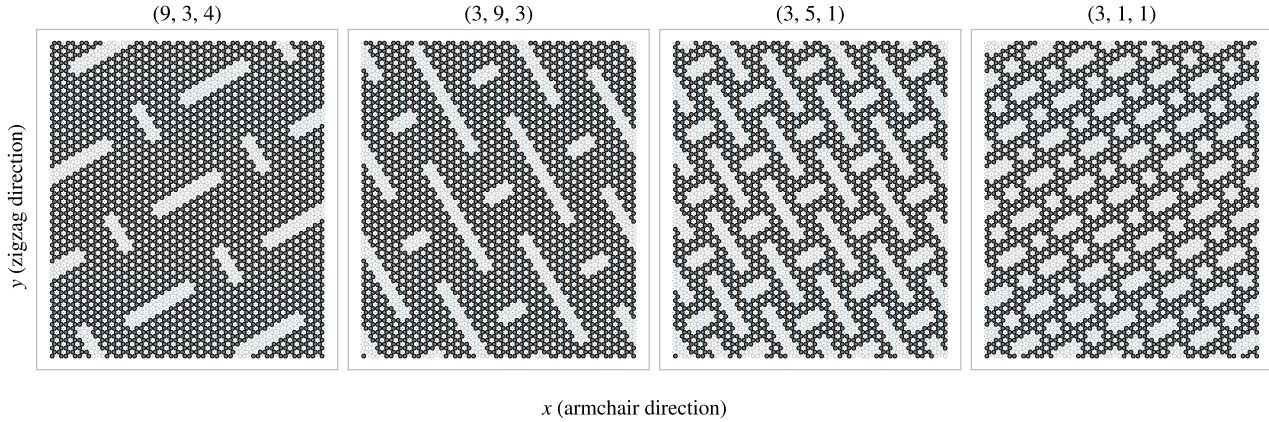


Figure 2.9: Sheet size used in example

2.5.2 Honeycomb

The *Honeycomb* pattern is defined, similarly to the Tetrahedron pattern, in terms of the center elements for which all surrounding atoms are removed. The Honeycomb pattern is build from a repeating series of cuts reminiscent of the roman numeral one rotated by 90° (I^\perp). For a given spacing these are put next to each other

¹The general formula for this number is rather complicated in comparison to the importance in this context. Thus, we exclude the formula for this calculation as the derivation is rather handwavy executed, but the number stated here is numerically backed for this specific parameter set.

in the x-direction, $\overbrace{\text{---}}^{\text{x}}$, to achieve a row where only a thin *bridge* in between is left to connect the sheet vertically in the y-direction. By placing multiple rows along the y-direction with alternating x-offset we get the class of honeycomb patterns as visualized in Fig. 2.10. The pattern is described in terms of the parameters: (x-width, y-width, bridge thickness, bridge length) which is annotated in Fig. 2.10a with the parameters (2, 2, 1, 5) used as an example. Some additional variations of the pattern class is showcased in Fig. 2.11.

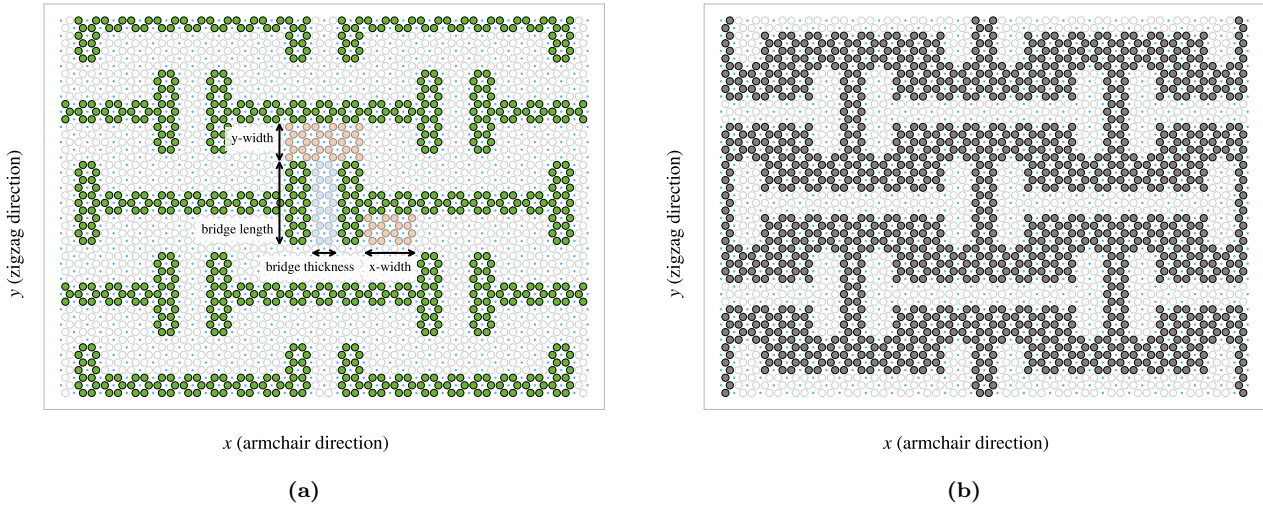


Figure 2.10

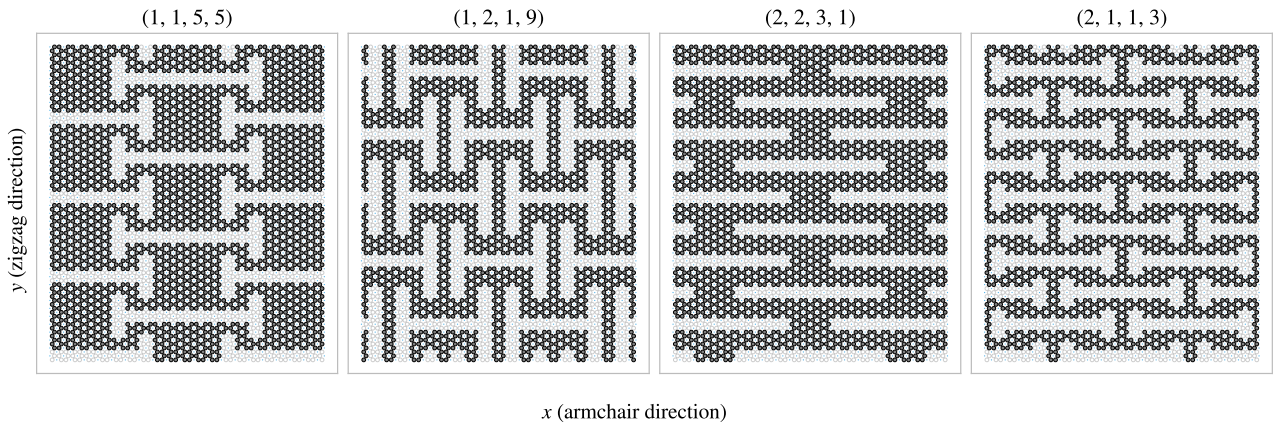


Figure 2.11

2.5.3 Random walk

The random walk serves as a method for introducing random patterns into the dataset with the scope of populating the configuration space more broadly than achieved purely with the more systematic patterns described above. By this argument, a straightforward way to create random configurations could be achieved simply by random noise, either uniform or gaussian. However, this would often leave the sheet detached with lots of non-connected atom clusters. Intuitively, we do not find this promising for the generation of large scale organized structures which we hypothesize to be of interest. The random walk pattern generation is characterized by the parameters summarized in Table 2.3 which will be introduced throughout the following paragraphs.

Table 2.3: Parameters for the random walk generator.

Parameters	Value	Description
Num. walkers (M)	Integer ≥ 1	Number of random walks to be initiated on the sheet (one at a time).
Max. steps (S)	Integer ≥ 1	The maximum steps allowed for any random walker.
Min. distance	Integer ≥ 0	The minimum distance required between any future paths and the previous paths in terms of the shortest walking distance in between.
Bias	(Direction, strength ≥ 0)	Bias direction and strength defining the discrete probability for the choice of the next site.
Connection	Atoms / Center elements	Whether to walk between atom sites or center elements (removing all adjacent atoms).
Avoid invalid	True/False	Whether to remove already visited sites from the neighbour list before picking the next site. This prevents jumping to already visited sites and lowers the likelihood of early termination.
Stay or break	$p = [0, 1]$	Probability that the walker will maintain its direction for the next step.
Periodic	True/False	Whether to use periodic boundary conditions on all four sides.
Avoid clustering	Integer ≥ 0	Amount of times to restart the whole random walk generation in order to arrive at a non-detached configuration. If no valid configuration is reached after this amount of tries, the non-spanning clusters are removed.
RN6	True/False	Randomly change the bias direction between the deployment of each random walker to one of the six center element directions.
Grid start	True/False	The option to have the random walkers start in an evenly spaced grid.
Centering	True/False	Relocate the path of a random walk after termination such that the path center of mass gets closer to the starting point (without violating the rules regarding already visited sites).

2.5.3.1 Fundamentals

For an uncut sheet we deploy M random walkers, one at a time, and let them walk for a maximum number of S steps. We can either let the walker travel between atom sites, removing the atoms in the path as it goes, or between center elements, removing all surrounding atoms — *Connection: Atom/Center elements*. The method of removing only the intersecting atoms between center elements was also incorporated, but we ended up not using it due to plenty of other interesting options. Nonetheless, we will always remove a site once visited such that the walker itself, or any other walkers, cannot use this site again. This corresponds with the property of a self avoiding random walk, but it furthermore constraint the walkers not to visit any path previously visited by others walkers which we might denote “other avoiding” then. By default, the walker has an equal chance of choosing any of its adjacent neighbours for the next step, i.e. we draw the next step from a discrete uniform distribution. Optionally we can use periodic boundary conditions, *Periodic: True/False*, allowing neighbouring sites to be connected through the edge in both the x and y-direction. When traveling on atom sites this ensures that we have three neighbour options for the next step while traveling on the center elements this gives six neighbour options. If the walker happens to arrive at an already visited site the walk is terminated early. Optionally, we can choose to remove any neighbouring sites already visited from the neighbour list, *Avoid invalid: True/False*, and choose uniformly between the remaining options instead. This prolongs the walking distance, but the walker

is still able to find itself in a situation where no neighbouring sites are available, note that it cannot backtrack its own path either, and in such a case the walk will be terminated despite the setting of *Avoid invalid*.

2.5.3.2 Spacing of walking paths

In order to control the spacing between the paths of the various walkers we implement a so-called, *minimum distance*: $0, 1, \dots$, parameter describing the spacing required between paths in terms of the least amount of steps. When a walker has ended its walk, either by early termination or hitting the maximum limits of steps, all sites within a walking distance of the minimum distance is marked as visited, although they are not removed from the sheet. This prevents any subsequent walkers to visit those sites in their walk according to the general behaviour introduced in the previous paragraph. In practice this is done through a recursive algorithm as described in algorithm Algorithm 1. For a given path the function *walk_distance()* is called with the input being a list of all sites in the given paths. For each site, the function then gathers all site neighbours (regardless of their state on the sheet) and call itself using this neighbour list as input while incrementing a distance counter passed along. This will result in an expansion along all possible outgoing paths from the initial path of interest which is terminated when the distance counter hits the distance limit. The function will then return the final neighbour lists which is cummulated into a final output corresponding to a list of all sites within the minimum distance to the path.

Algorithm 1 Recursive algorithm implemented as class method to mark sites within a distance of the class attribute *self.min_dis*.

```

Require: self.min_dis > 0                                ▷ This pseudocode does not handle other cases
1: function WALK_DISTANCE(self, input, dis = 0, pre = [ ])      ▷ Initialize list for new neighbours
2:   new_neigh ← [ ]
3:   for site in input do
4:     neigh ← get_neighbouring_sites(site)                      ▷ Get sourrounding neighbours
5:     for n in neigh do
6:       if (n not in pre) and (n not in new_neigh) then          ▷ If not already added
7:         AddItem(new_neigh, n)
8:       end if
9:     end for
10:    end for
11:    dis += 1                                              ▷ Increment distance counter
12:    if dis ≥ self.min_dis then                            ▷ Max limit hit
13:      return input + new_neigh
14:    else                                                 ▷ Start a new walk from each of the neighbouring sites
15:      pre ← input
16:      return pre + self.walk_distance(new_neigh, dis, pre)
17:    end if
18: end function

```

Do we need a figure supporting this?

2.5.3.3 Bias

We include the option to perform biased random walk through the Bias: (direction, strength) parameter option. We implement this by modelling each walking step analog to the canonical ensemble under the influence of an external force \mathbf{F} representing the bias. For such a system each microstate i , corresponding to the sites in the neighbour list, has the associated probability p_i given by the Gibbs–Boltzmann distribution

$$p_i = \frac{1}{Z} e^{-\beta E_i}, \quad Z = \sum_i e^{-\beta E_i},$$

where Z is the canonical partition function, $\beta = 1/k_B T$ for the boltzmann constant k_B and temperature T , and E_i the energy of site i . We model the energy of each site as the work required to move there. For a step s the energy becomes $E_i = -s \cdot \mathbf{F}$, where the sign is chosen such that the energy (difference) is negative when moving

for aligning the bias, analogous to an energy gain by moving there. Due to the symmetry of both the atom sites and the center elements sites the step length to neighbouring sites will always be equal. By defining the bias magnitude $B = \beta|\mathbf{F}||\mathbf{s}|$ we get the probability for jumping to site i as

$$p_i = \frac{1}{Z} e^{B\hat{\mathbf{s}} \cdot \hat{\mathbf{F}}} \propto e^{B\hat{\mathbf{s}} \cdot \hat{\mathbf{F}}},$$

where the hat denotes the unit direction of the vector. The bias magnitude B then captures the opposing effects of the magnitude of the external force and the temperature of the system as $B \propto |\mathbf{F}|/T$. We notice that $\hat{\mathbf{s}} \cdot \hat{\mathbf{F}} = \cos(\theta)$ for the angle θ between the step and bias direction. This shows that the bias will have the biggest positive contribution to the probability when the step direction is fully aligned with the bias direction ($\theta = 0$), have no contribution for orthogonal directions ($\theta = \pm\pi/2$) and the biggest negative contribution when the directions are antiparallel ($\theta = \pi$). The partition function serves simply as a normalization constant. Thus, numerically we can enforce this simply by setting $Z = 1$ at first, calculate p_i , and then normalize the result at the final stage as a division by the sum of all p_i . In the numerical implementation we then pick the step destination weighted by the discrete probability distribution p_i . In Fig. 2.12 we have illustrated how a bias of different strength impacts the probability distribution for a random walk between center elements. We can visually confirm that the bias will favorize the directions that lies closer to the bias direction. This favorization is more distinct at high bias strengths while at low strength $B \rightarrow 0$ we get a uniform distribution which aligns with the default unbiased random walk.

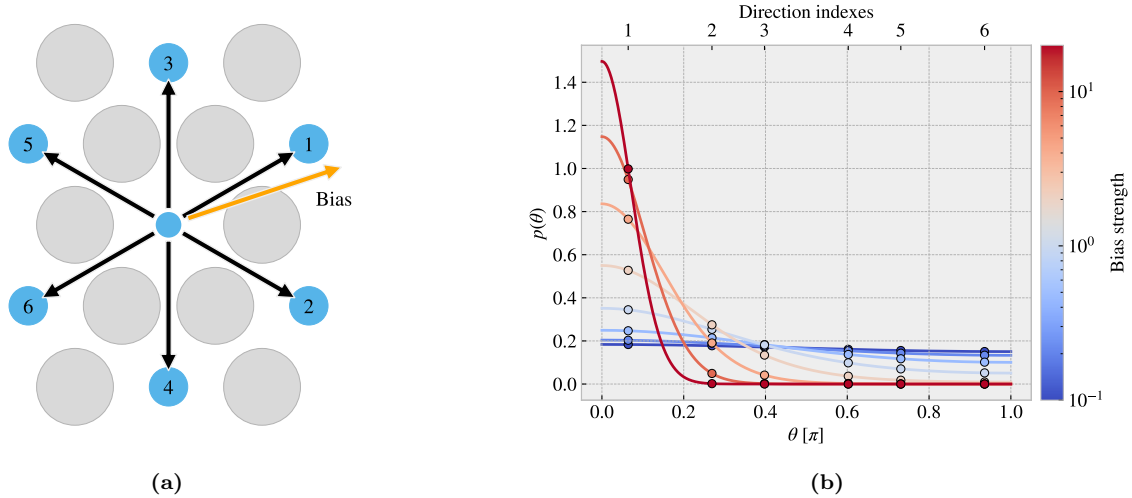


Figure 2.12: Illustration of the probability distribution for the various step direction during a bias random walk between center elements. (a) Shows the possible step directions as black arrows pointing towards the neighbouring center elements shown as blue circles. The bias direction is denoted as an orange arrow and the numbering indicates the most likely direction to take (1) towards the least likely (6). The atoms sites are marked as grey circles for reference. (b) The probability distribution as a function of angle between the direction of choice and the bias direction. The distribution is normalized according to the discrete probabilities marked with dots for which the continuous line simply highlights the curve of the distribution. The direction indexes corresponds to the numbering on figure (a). The color map indicates different strengths of the bias.

2.5.3.4 Stay or break

The *Stay or break: True/False* parameter defines the probability p_{stay} that the walker will keep its direction or otherwise break into a different direction by probability $1 - p_{\text{stay}}$. That is, we manually substitute p_{stay} in the discrete probability for the next step corresponding to a continuation in the same direction. We then shift the remaining probabilities such that the distribution remains normalized. In this way we can still perform bias random walk in combination. For the center element walk it is trivial to determine which of the neighbour directions correspond to a continuation of direction based on the last visited site. However, for an atom site walk, it is not possible to follow the same direction in a straight line due to the hexagonal layout of the lattice.

We recall that the nearest atom neighbour indexes alternates for each increment in x or y index (see Eq. (2.1)) which corresponds to the alternating neighbour directions D

$$(i+j) \text{ is even} \rightarrow D = \left\{ \frac{a}{2} \left(\frac{-2}{\sqrt{3}}, 0 \right), \frac{a}{2} \left(\frac{1}{\sqrt{3}}, 1 \right), \frac{a}{2} \left(\frac{1}{\sqrt{3}}, -1 \right) \right\},$$

$$(i+j) \text{ is odd} \rightarrow D = \left\{ \frac{a}{2} \left(\frac{2}{\sqrt{3}}, 0 \right), \frac{a}{2} \left(\frac{-1}{\sqrt{3}}, 1 \right), \frac{a}{2} \left(\frac{-1}{\sqrt{3}}, -1 \right) \right\}.$$

One way to mitigate this issue is to use the six directions from the center element walk as the common direction to “stay or break” from. As showcased in Fig. 2.13, for each center element direction (black arrows) there are two possible atom directions (red and orange arrows) that are equally close to the center element direction. The red and orange arrows represent $(i+j)$ being even or odd respectively, and we notice that these appear in pairs such that we can always determine which of the atom directions that are closest to the center element direction. Following this idea we can map each center direction to an atom direction depending on the even or oddness of the position. For $p_{\text{stay}} = 1$ this results in a guaranteed zigzag motion along the center element direction that it happens to start on.

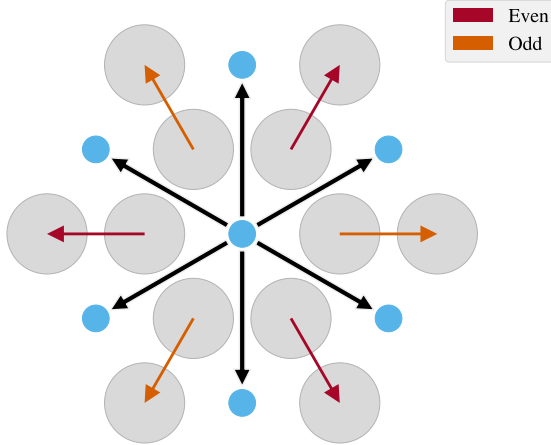


Figure 2.13: Caption

The *Stay or break* is still subject to previously defined rules, such that in the case that the site preferred site is not available, it will either terminate when going there, or it is removed from the neighbour list when *avoid unvalid: True*. For the latter case the walker has broken its direction and will follow the new direction with probability p_{stay}

2.5.3.5 Deployment schemes

By default, each random walker is given an uniform random starting point among the non-visited available sites left on the sheet. This includes any modifications in relation to the minimum distance parameter. By toggling the *Grid start: True/False* parameter on, the starting points are instead predefined on an evenly spaced grid. That is, the sheet is subdivided into the least amount of squares that will accommodate a space for each starting point. 1 walker leads to a 1×1 partition, $\{2, 3, 4\}$ walkers lead to a 2×2 partition, $\{5, 6, 7, 8, 9\}$ walker lead to a 3×3 partition and so on. For each partition square the starting point is placed as central as possible. The lower left partition square is then chosen as a default starting place for the first walker and the remaining sites are filled according to the order that maximizes the minimum distance between a new starting point and the ones already used². The population of the grid is visualized in Fig. 2.14 for 1-9 walkers in total with color coding for the order of deployment.

²In hindsight, it would have been less biased to choose a random partition square, but we do not consider this to be of great importance for the usage of this feature in final dataset

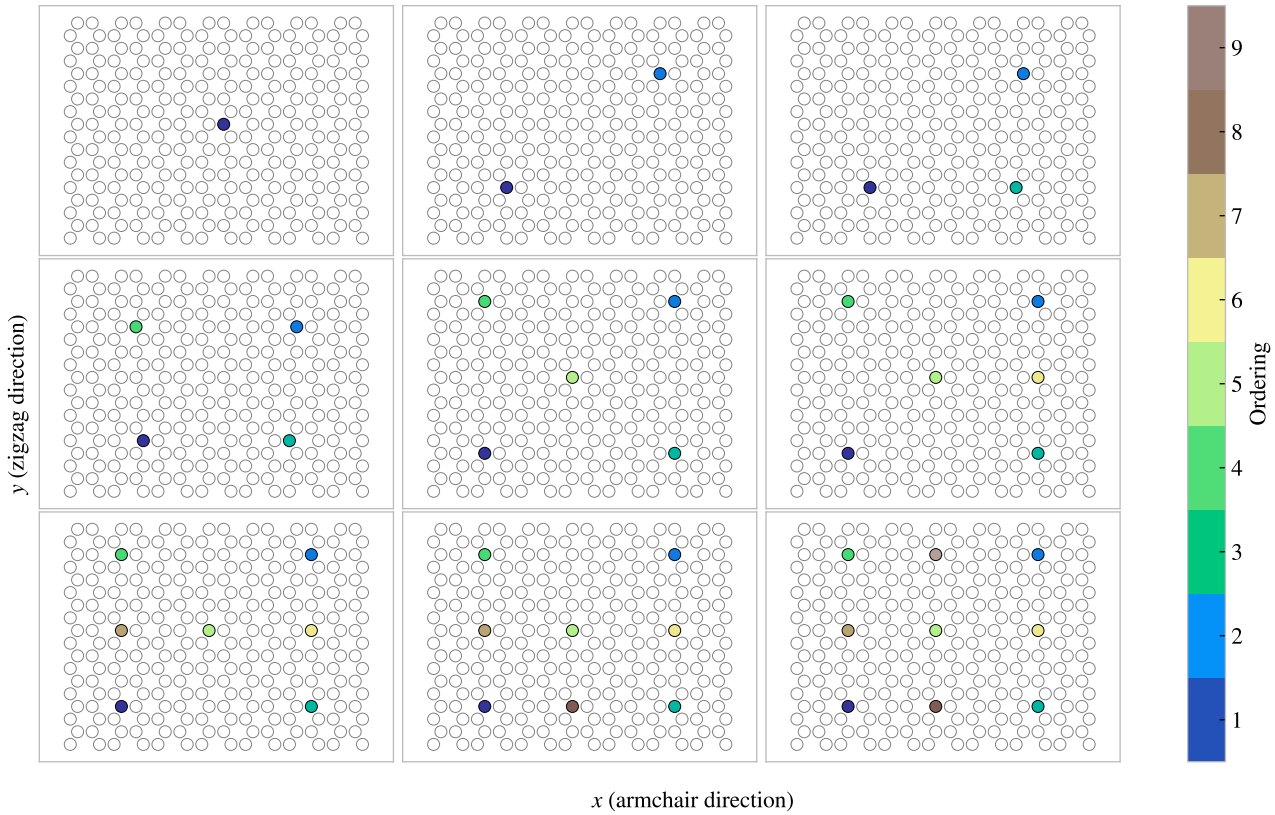


Figure 2.14: Population of starting points with the centering parameter toggled on in a 14×18 sheet. This is shown for 1-9 number of random walkers with the color map conveying the order of the population.

The *Centering: True/False* parameter let us relocate the path of the random walker such that the path center of mass aligns better with the starting point. When toggled on, the path is moved in the direction defined by the center of mass and the starting point for which the closest valid relocation on the direct translation line is chosen. This can be used in combination with the grid start and the bias parameter to make rather ordered configurations. In addition, the *RN6:True/False* parameter can be used update the bias direction to on of the six directions of the center element walk for each new walker deployed. This lets us create configurations like the one shown in Fig. 2.15b.

2.5.3.6 Validity

The simulation procedure requires the sheet to be fully attached, non ruptured, which can be summarized as the following requirements.

1. There exist only a single cluster on the sheet. We define a cluster as the set of atoms which can all be reached through nearest neighbour walking on the cluster.
2. The cluster of atoms is spanning the sheet in the y-direction. This means that there exist at least one path through nearest neighbour walks that connect the bottom and the top of the sheet. This is due to the reason that the sheet must be attached to the pull blocks.

In order to accommodate these requirements we count the number of clusters and search for a spanning cluster after all walkers have terminated. If the requirements are not met we simply rerun the random walk from scratch. This is done, *Avoid clustering: 0, 1, ..., amount of times*. If the requirements are not met during any of those reruns the non-spanning clusters are simply removed. In the case of no spanning cluster the configuration is skipped. This crude scheme was later reinvented as a more refined repair scheme which alters the sheet by the intention of performing the least amount of changes (addition or subtraction of atoms) in order to meet the attachment requirements. This was done as a part of the accelerated search procedure and hence it was not utilized in the creation of the random walk dataset.

2.5.3.7 Random walk examples

Some examples of the random walk patterns are illustrated in Fig. 2.15.

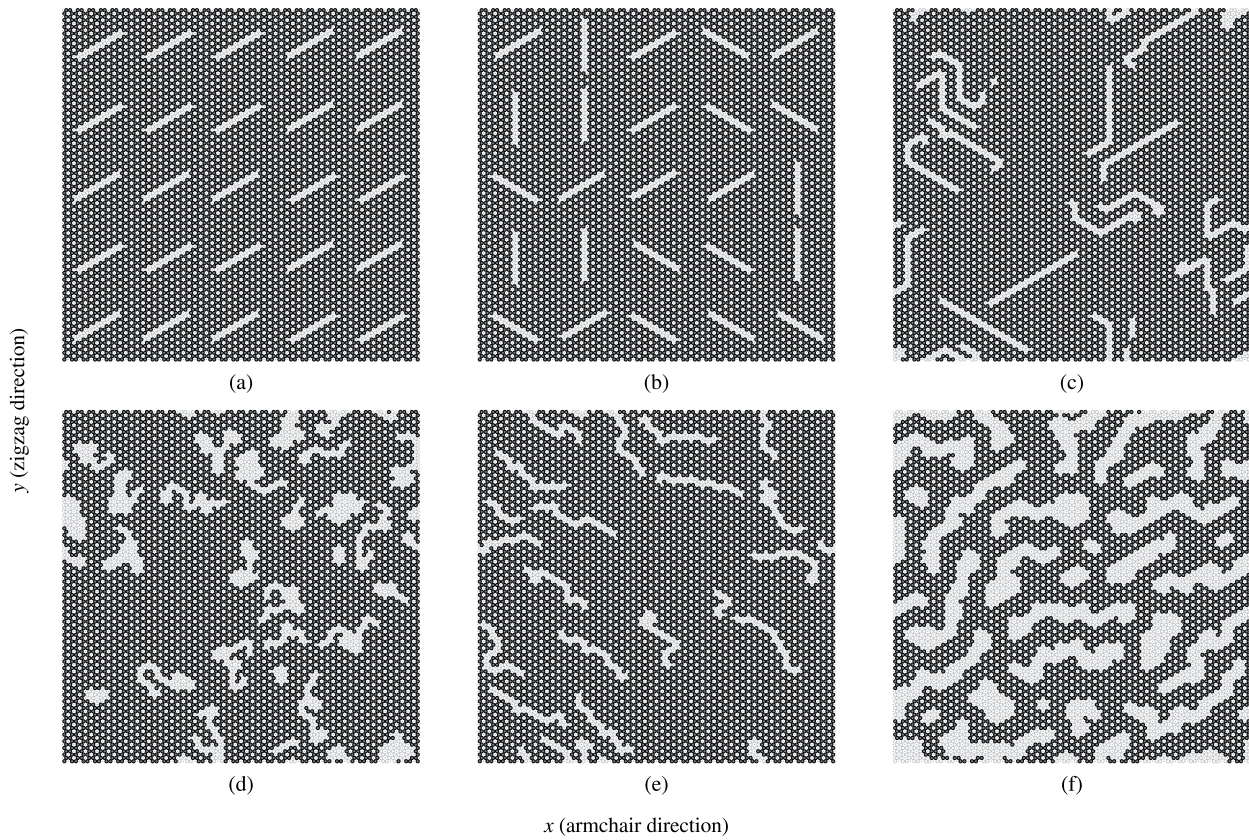


Figure 2.15: Some example uses of the random walking class. Give information of parameters?

Chapter 3

Pilot study

Having defined our system, we carry out an initial study of the numerical approach. This includes an analysis of how to define and measure the frictional properties of interest, and an investigation of the main parameters governing the numerical solutions. From this point of view we decide on suitable parameters for the remaining study. Particularly, we investigate the frictional behaviour under the variation of load and stretch for a selected set of configurations which serves as a baseline for later comparison and an assessment of the prospects of Kirigami modifications for friction.

3.1 Friction simulation parameters

The MD simulation is governed by a small set of parameters, some which are related directly to the numerical aspects of the simulation and other related to the physical conditions we are simulating. Thus, we differentiate between the two main categories: 1) *Physical*, parameters which alter the physical conditions of the “numerical experiment” and are expected to effect the frictional behaviour. 2) *Numerical*, parameters which are related more closely to the numerical procedure itself, expected to influence the simulation dynamics, which should be chosen to ensure the most stable results. For the purpose of creating the machine learning dataset most of these parameters will be kept constant with only a subset of the physical parameters being varied. The parameters are summarized in Table 3.1 where the grey shaded area marks the parameters, Configuration, stretch and load, which we will vary for the dataset. Due to the great number of parameters it is unreasonable to make an exhaustive search of all parameters before deciding on the final settings. Instead, we take a basis in the parameters used in similar studies [SOURCES](#) and adjust them as we carry out the initial analysis of the simulation results. Thus, we start at values most representative for other similar simulations and adjust according to the stability of the results and the computation time. Since we are going to introduce a lot of complexity to the system, through the cut and stretch deformation, we are less concerned about aligning parameters for comparison. Instead of presenting the process of narrowing down the final parameters in a chronological manner, we have shown the final choice shown in Table 3.1 which we will discuss throughout the following presentation of the pilot study. Notice, that the values in Table 3.1 serve as default values which are used when nothing else is stated.

Table 3.1: Parameters of the numerical MD simulation for measuring friction. The values correspond to the final choice used for the dataset. The shaded area denote the parameters varied in the ML dataset.

Category	Parameter	Value	Description
Physical	T	300 K	Temperature.
	v_{slide}	20 m/s	Sliding speed for the sheet translation.
	K	inf	Spring constant for the coupling between the virtual atom and the sheet pull blocks.
	Scan direction	$(x, y) = (0, 1)$ (zigzag direction)	The direction for which we translate the sheet.
	Sheet configuration	Contiguous	Binary mapping describing which atoms are removed (0) and which is still present (1) in the graphene sheet.
	Stretch amount	0% - rupture	The relative stretch of the sheet.
	F_N	[0.1, 10] nN	Applied normal force to the pull blocks.
Numerical	dt	1 fs	Integration timestep.
	t_R	15 ps	Relaxtion time before strething.
	Pauses	5 ps	Relaxtion pauses after stretch, and during the normal load phase (before translating the sheet).
	Stretch Speed	0.01 ps^{-1}	The rate of stretching for the sheet.
	Slide distance	400 Å	How far to translate the sheet.
	Sheet size	$130.029 \times 163.219 \text{ \AA}$	Spatial 2D size of the sheet.
	Pull block size	$2 \times 130.029 \times 15.183 \text{ \AA}$	Spatial 2D size of the pull blocks.

3.2 Force traces

We begin by assessing the friction force traces, i.e. force vs. time curves, for a single friction simulation using the default parameters shown in ?? for a non-cut sheet with no stretch applied and a normal load of 1 nN.

3.2.1 Force oscillations

We evaluate the friction force as the force acting on the sheet from the substrate. We consider initially the force componenet F_{\parallel} parallel to the drag direction as plotted in Fig. 3.1. We use a sample rate of $10 \text{ ps}^{-1} = 100 \text{ timesteps}^{-1}$ for which each sample is the mean value of the preceding 100 timesteps. We observe immediately that the data carriers oscillations on different time scales matching our general expectations for sliding involving periodic surfaces. By applying a savgol filter to the data with a polyorder of 5 and window length of 150 timesteps (corresponding to a sliding distance of 3 Å or a time window of 15 ps) we can qualitatively point out at least two different frequencies of oscylation. During the first 10 Å of sliding, seen in Fig. 3.1a, we see roughly three waves on the savgol filter corresponding to a relative high frequency, while for the duration of 100 Å of sliding, seen in Fig. 3.1b, the same savgol filter reveals a lower frequency on top, creating the visual pattern of a wavepacket. The data does not indicate clear signs of stick-slip behaviour as otherwise found in other studies, e.g. by Zhu and Li [17] for graphene on gold, who saw a more typical saw tooth shape in the force trace. Beside the difference in substrate material, using gold instead of silicon, they used a lower sliding speed of 10 m/s and a soft spring of $K = 10 \text{ N/m}$. By adopting those parameters we get a slightly different force trace behaviour as shown in Fig. 3.1c and Fig. 3.1d. This change breaks the symmetry in the force oscillations, but still does not produce any significant discontinuities in the trace. By keeping the spring constant $K = 10 \text{ N/m}$ and lowering the sliding speed further down to 1 m/s we are able to demonstrate a proper stick-slip behaviour as shown in Fig. 3.1e and Fig. 3.1f. Considering all three simulations we might classify the results from the default settings, $K = \text{inf}$, $v = 20 \text{ m/s}$, as smooth sliding, $K = 10 \text{ N/m}$, $v = 10 \text{ m/s}$, as a transistion phase with possible occasional slipping, and $K = 10 \text{ N/m}$, $v = 1 \text{ m/s}$ as certain stick-slip behaviour.

Refer a bit to theory on this one

However, the low sliding speed comes with a high computational cost which is the reason that we choose a sliding speed of 20 m/s. The choice of an infinite spring constant is related to the stability of the measurements as discussed later [make reference](#).

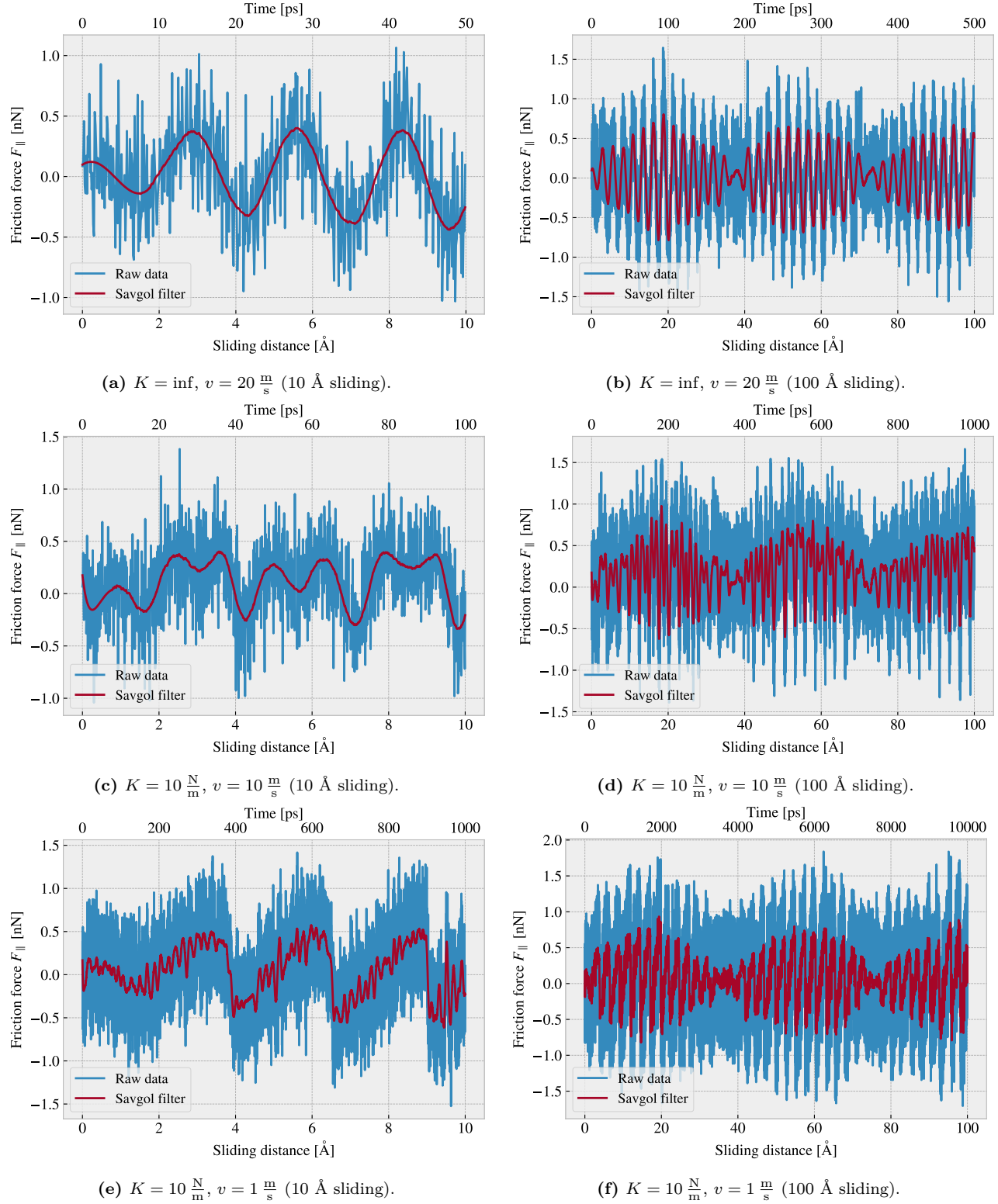


Figure 3.1: Force traces of the friction force F_{\parallel} with respect to the drag direction between acting from the substrate on the full sheet and substrate. The force traces is plotted against the sliding distance (lower x-axis) and the corresponding sliding time (upper x-axis). The sliding distance is measured by displacement of the virtual atom tethering the sheet. The red line represents a savgol filter with window polyorder 5 and window length of 150 timesteps (corresponding to a sliding distance of 3 \AA or a time window of 15 ps). Each row, (a,b), (c,d), (e,f), represents a different choice of the spring constant K and sliding speed v , while the columns show the same result for two different time scales. The default settings are represented in figure (a) and (b).

By performing a Fourier Transform on the data, using the default parameters, we can quantify the leading frequencies observed in figure Fig. 3.1a and Fig. 3.1b. The Fourier transform is shown in Fig. 3.2a, and by plotting the two most dominant frequencies $f_1 = 0.0074 \text{ ps}^{-1}$ and $f_2 = 0.0079 \text{ ps}^{-1}$ as a sine sum, $\sin(2\pi f_1) + \sin(2\pi f_2)$, we find a qualitatively convincing fit to the observed wavepacket shape as seen in Fig. 3.2b. We can convert the frequencies according to that of a wavepacket. By using the trigonometric identity

$$\begin{aligned}\sin(a+b) &= \sin(a)\cos(b) + \cos(a)\sin(b), \\ \sin(a-b) &= \sin(a)\cos(b) - \cos(a)\sin(b),\end{aligned}$$

and decomposing the frequencies as $f_1 = a - b$, $f_2 = a + b$, we can rewrite the sine sum as the sinusoidal product

$$\begin{aligned}\sin(2\pi f_1) + \sin(2\pi f_2) &= \sin(2\pi(a-b)) + \sin(2\pi(a+b)) \\ &= \sin(2\pi a)\cos(2\pi b) + \cancel{\cos(2\pi a)\sin(2\pi b)} + \sin(2\pi a)\cos(2\pi b) - \cancel{\cos(2\pi a)\sin(2\pi b)} \\ &= 2\sin(2\pi a)\cos(2\pi b),\end{aligned}$$

with

$$\begin{aligned}a &= \frac{f_1 + f_2}{2} = 0.0763 \pm 0.0005 \text{ ps}^{-1}, & b &= \frac{f_2 - f_1}{2} = 0.0028 \pm 0.0005 \text{ ps}^{-1}, \\ &= 0.381 \pm 0.003 \text{ \AA}^{-1}, & &= 0.014 \pm 0.003 \text{ \AA}^{-1},\end{aligned}$$

where the latter frequency is denoted with respect to the sliding distance. This makes us recognize the high oscillation frequency as a and the low frequency as b . The faster one has a period of $T_a = 2.62 \pm 0.02 \text{ \AA}^3$ which corresponds well with the magnitude of the lattice spacing and especially that of graphene at 2.46 \AA as expected theoretically. The longer period $T_b = 71 \pm 15 \text{ \AA}^{-1}$ is not obviously explained. We noticed a similar long period oscillation for all three cases, Fig. 3.1b, Fig. 3.1d and Fig. 3.1f, regarding stick-slip behaviour, and thus we do not believe that this is directly related. The initial build up in friction force is reminiscent of a friction strengthening, which is often reported SOURCE, but the periodicity goes against this idea. Instead, we might attribute it to some kind of phonon resonance which could be a physical phenomenon or simply a feature of our MD modelling.

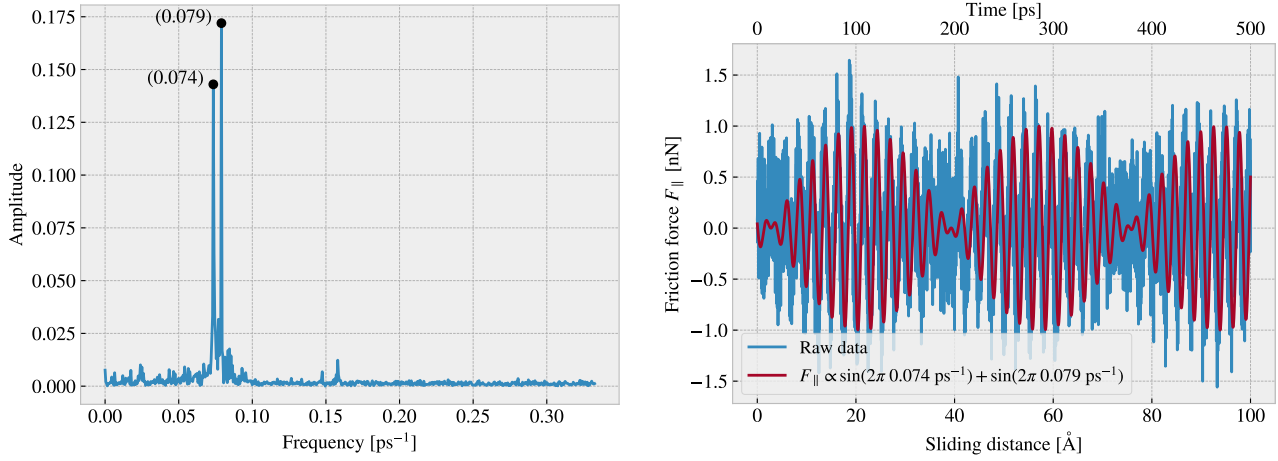


Figure 3.2: Fourier transform analysis of the full friction force data (all 400 \AA sliding distance) shown in Fig. 3.1. (a) shows the two most dominant frequency peaks. Note that no significant peaks were found in a higher frequency than included here. (b) shows a comparison between the raw data and the wavefunction corresponding to the two peaks in figure (a).

³The uncertainty Δy is calculated as $\Delta y = \left| \frac{\partial y}{\partial x} \Delta x \right|$ for uncertainty Δx and $y(x)$

3.2.2 Decompositions

In the previous analysis we have looked only at the friction force for the full sheet, including the rigid pull blocks, and with respect to the drag direction. We found this way of measuring the friction force to be the most intuitive and reliable, but we will present the underlying arguments for this choice in the following.

Due to the fact that we are only applying cuts to the inner sheet, and not the pull blocks, it might seem more natural to only consider the friction on that part. If the desired frictional properties can be achieved by altering the inner sheet one can argue that any opposing effects from the pull blocks can be mitigated by simply scaling the relative size between the inner sheet and the pull blocks. However, when looking at the force traces decomposed with respect to the inner sheet and pull block regions respectively, see Fig. 3.3a, we observe that the friction force arising from those parts are seemingly antisymmetric. That is, the distribution of the frictional pull from the substrate on the sheet is oscillating between the inner sheet and the pull block. Keeping in mind that normal force is only applied to the pull blocks we might take this as an intrinsic feature of the system which does not necessarily disappear by scaling of the spatial ratio between the inner sheet and pull block. Any interesting friction properties might depend on this internal distribution of forces. Hence, we hedge our bets and use the full sheet friction force as a holistic approach to avoid excluding relevant information in the measurement data.

Similar we might question the decision of only considering the frictional force projected onto the sliding direction as we are then neglecting the “side shift” induced during sliding. In Fig. 3.3b we show the decomposition in terms of force components parallel F_{\parallel} and perpendicular F_{\perp} to the sliding direction respectively. We notice that the most dominant trend appears for the parallel component. If we want to include the perpendicular component as well we would have to evaluate friction as the length of the force vector instead, but this would remove the sign of the force direction and shift the mean friction force up as we clearly see both negative and positive contributions in the parallel force trace. One option to accommodate this issue is by using the vector length for the magnitude but keeping the sign from the parallel component. However, we omit such compromises as this might make the measurement interpretation unnecessary complex, and we use only the parallel component going forward.

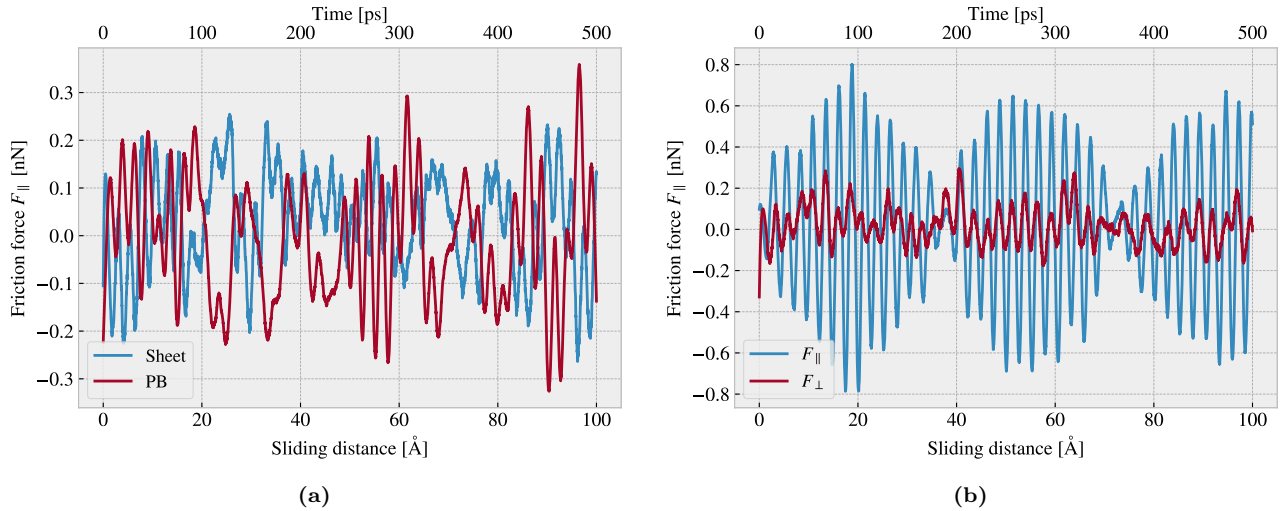


Figure 3.3: Friction force decomposition on the default parameter force trace shown in Fig. 3.1 showing only the applied savgol filters. (a) Decomposition into group inner sheet (sheet) and pull blocks (PB). (b) Decomposition into parallel (F_{\parallel}) and perpendicular (F_{\perp}) to drag sliding direction.

3.2.3 Center of mass path

From the previous observations of the force traces Fig. 3.1 we demonstrated both smooth sliding and stick-slip behaviour. Considering the force decomposition in Fig. 3.3b we know that the frictional forces in the perpendicular direction to sliding is also present. By looking at the x, y -position for the sheet Center of Mass (CM) we see a qualitatively different behaviour when reconsidering the spring constant and sliding speed investigated in Fig. 3.1 which is shown in Fig. 3.4. The default case in Fig. 3.4a shows a rather straight path forward with only a

small side motion in comparison to the cases in Fig. 3.4b and Fig. 3.4c. However, the CM accelerates and deaccelerates with a high frequency, much too high to be associated with the lattice spacing on the order of 2.46 Å (interatomic distance of 1.42 Å). One possible explanation is that the sheet and substrate constitutes an incommensurable contact for which travelling kink excitations make the atoms move in such a way that the sheet CM is incremented in small “burst”. When looking at the $K = 10 \frac{\text{N}}{\text{m}}$, $v = 10 \frac{\text{m}}{\text{s}}$ case in Fig. 3.4b we see a completely different CM path where the rapid parts aligns visually better with the force oscillations shown earlier in Fig. 3.1d. The CM accelerates forward and the deaccelerates in combination with a side motion that lead to the CM path making a loop as it slows down. Finally we have the $K = 10 \frac{\text{N}}{\text{m}}$, $v = 1 \frac{\text{m}}{\text{s}}$ in Fig. 3.4b which is confirmed to have stick-slip behaviour in Fig. 3.1f. Here the CM path shows a more chaotic movement between acceleration which also aligns visually well with the timing of the slips seen in Fig. 3.1f. The chaotic motion is not obviously connected to the stick-slip motion, but we omit a further investigation as this is not corresponding to the parameters that we will be using.

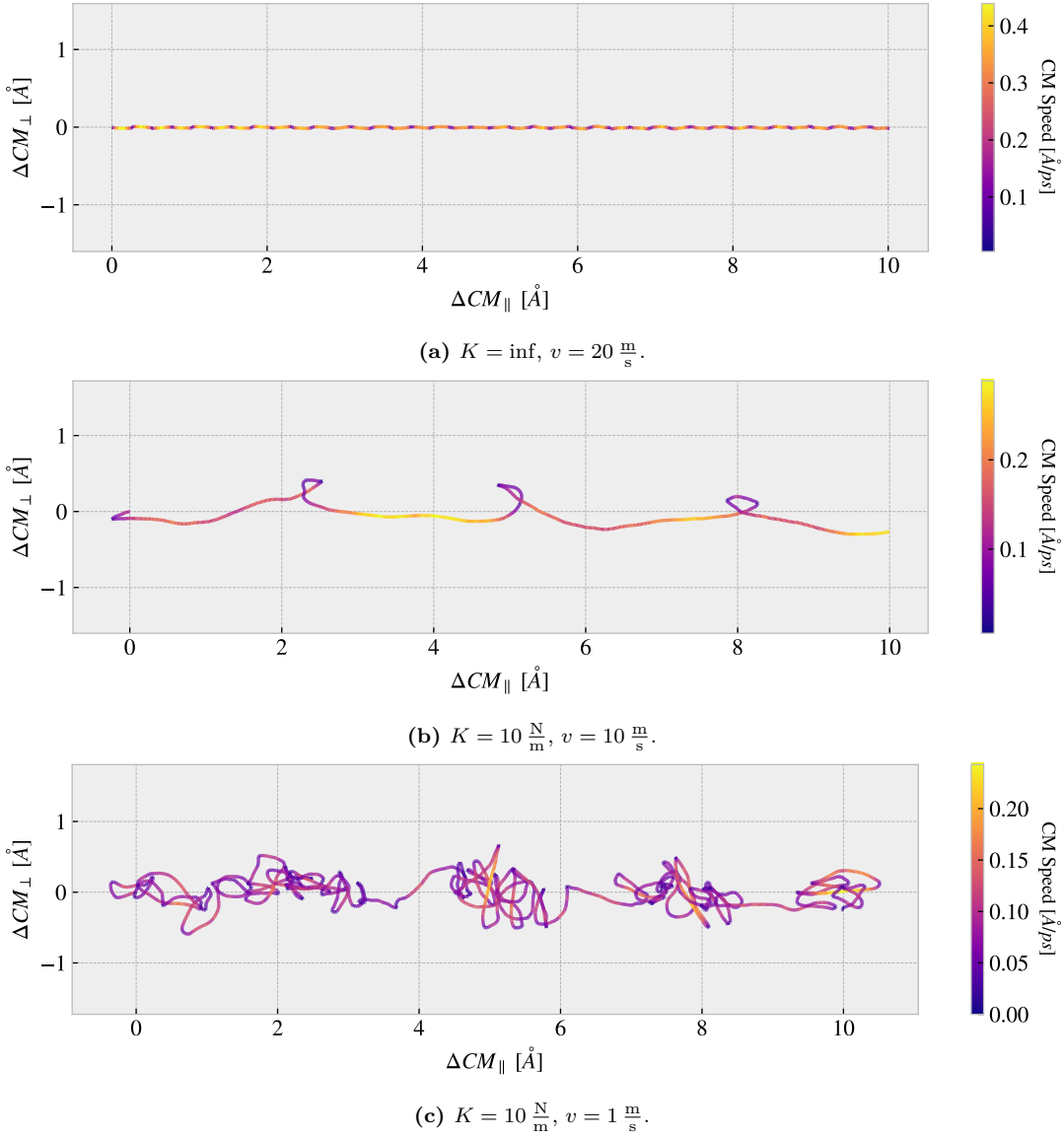


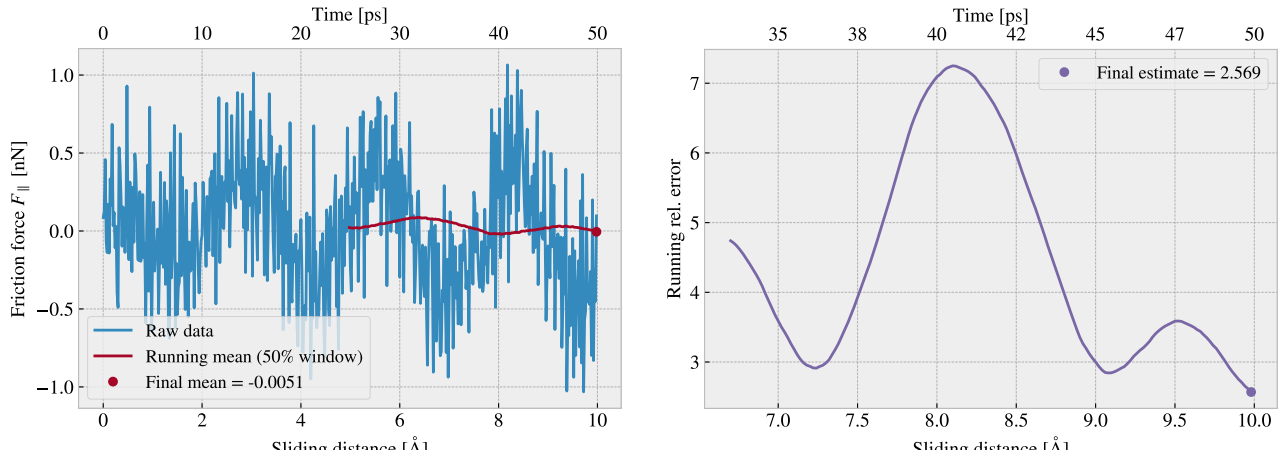
Figure 3.4: Center of Mass (CM) position relative to the start of the sliding phase in terms of the direction parallel to the sliding direction ΔCOM_{\parallel} and the axis perpendicular to the sliding direction ΔCOM_{\perp} . The colorbar denotes the absolute speed of the CM motion. Figure a-c shows different parameters used for the spring constant K and sliding speed v similar to that used in Fig. 3.1. (a) Default: $K = \infty$, $v = 20 \frac{\text{m}}{\text{s}}$. (b) $K = 10 \frac{\text{N}}{\text{m}}$, $v = 10 \frac{\text{m}}{\text{s}}$. (c) $K = 10 \frac{\text{N}}{\text{m}}$, $v = 1 \frac{\text{m}}{\text{s}}$

3.3 Defining metrics for friction

In order to evaluate the frictional properties of the sheet we aim to reduce the force trace results, addressed in section Sec. 3.2, into single metrics describing the kinetic and static friction respectively.

3.3.1 Kinetic friction

We measure kinetic friction as the mean of the friction force trace. More precisely, we take the mean value of the latter half of the dataset in order to ensure that we are sampling from a stable system. For a full sliding simulation of 400 Å we thus base our mean value on the latter 200 Å (1000 ps) of sliding. In Fig. 3.5a we have shown the force trace for the first 10 Å of sliding together with a 50% running mean window. The choice of such a short sliding distance is merely to illustrate the sampling procedure, and we see that the final mean estimate (marked with a dot) takes a negative value due to the specific cut-off of the few oscillations captured here. Nonetheless, one approach to quantify the uncertainty of the final mean estimate is to consider the variation of the running mean preceding the final mean value. The more the running mean fluctuates the more uncertainty associated with the final estimate. Only the running mean “close” to the ending should be considered, since the first part will rely on data from the beginning of the simulation. From the Fourier analyse in section Sec. 3.2.1 we found the longest significant oscillation period to be $\sim 71 \text{ \AA}^{-1}$ corresponding to $\sim 35\%$ of the running mean window which gives a window length of 200 Å when including all the data. Hence, we use the standard deviation of the final 35% of the running mean to approximate the uncertainty of the final mean value. We consider the standard deviation (std) as an estimate of the absolute error and calculate the relative error by a division of the final mean value. In Fig. 3.5b we showcase a running relative error based on the std, with a window of length 35% the mean window, in a continuation of the illustrative case of a 10 Å sliding from Fig. 3.5a. In this case we get an extremely high relative error of $\sim 257\%$, but this is desirable since the sampling period leads to an unphysical negative value which should be associated with a high uncertainty.



(a) Running mean with window length 5 Å (50% the data length). (b) Running std with window length 1.75 Å (35% the mean window length.)

Figure 3.5: Running mean (a) and running relative error (std) (b) on the friction force data from a reduced sliding distance of 10 Å. The running mean window is 50% the data length while the running std window is 35% the running mean window length. The values are plotted at the end of their respective windows such that window precedes the actual point on the graph.

When including the full dataset of 400 Å of sliding, such that the std window actually matches with the longest period of oscillations expected, we get a final relative error of $\sim 12\%$ as shown in fig Fig. 3.6. This is arguable just at the limit of an acceptable error, but as we shall see later on in Sec. 3.6 this high relative error is mainly associated with the cases of low friction. When investigating different configurations under variation of load and stretch we see a considerable lower relative error as the mean friction evaluates to higher values. One interpretation of this finding is simply that the oscillations in the running mean are to some degree independent of

the magnitude of the friction. In that case, the relative error will spike for the low friction cases, and the absolute error might be there more reliable measure, i.e. taken simple the std without dividing by the final mean value.

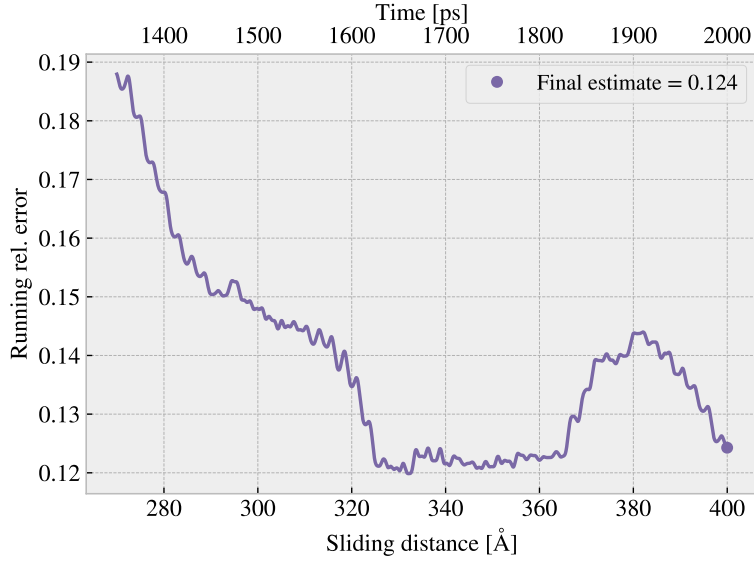


Figure 3.6: Running standard deviation (std) for a full 400 Å sliding simulation. The running std window is 70 Å (35% the running mean window of 50% the data length).

3.3.2 Static friction

The maximum value is one of the common choices for addressing static friction, even though the definition of static friction is a bit vague. When considering the force traces in Fig. 3.1 we observe that the force oscillations increase in magnitude toward a global peak at ~ 20 Å. Thus, one could be inclined to identify this peak as the maximum value associated with the static friction force. However, as we have already clarified, this steady increase in friction is a part of a slower oscillation which repeats by a period of ~ 71 Å $^{-1}$. By plotting the top three max values recorded during a full 400 Å simulation, for 30 logarithmically spaced load values in the range [0.1, 100] nN, we observe that the global max in fact rarely fall within this first oscillation period as shown in Fig. 3.7. Only 2/30 global maxima and 4/90 top three maxima can be associated to the start of the sliding by this definition. Thus, this result suggests that our default system does not yield a static friction response in the sense of an initial increase in friction due to a depinning of the sheet from the static state **Is this probably defined in the theory section?** Some parameter changes that might increase the likelihood of seeing a significant static friction response is either extending the relaxation period, as static friction is theorized to increase logarithmically with time, or to increase the sliding force more slowly and through a soft spring tethering. As an attempt to test parts of this hypothesis we run a series of simulations with varying spring constant, $K \in [5, 200]$ nN including also $K = \text{inf}$, but keeping the relaxation time and sliding speed at the default values. The result is shown in Fig. 3.8. The results do not show any support of the hypothesis that a softening of the spring constant will eventually lead to the maxima occurring in the first period of sliding. We note that this might be suppressed by having a too short relaxation period or a too high sliding speed, related to the rate of which force increased initially, but due to the ambiguousness in the assessment of the static friction we will mainly concern ourselves with the kinetic friction in the remaining of this thesis.

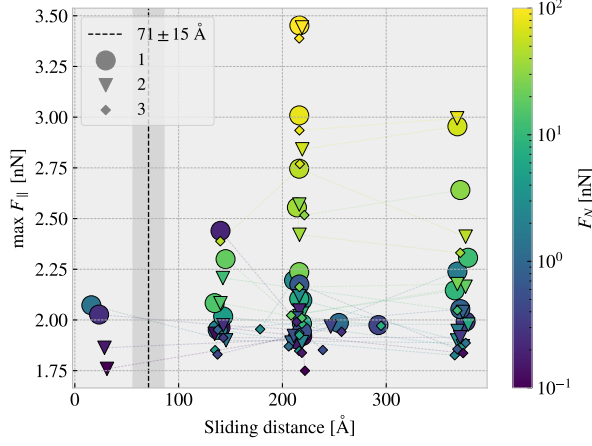


Figure 3.7: Distribution of top three max friction force peaks for 30 uniformly sampled normal forces $F_N \in [0.1, 10]$ nN. The dotted line and the grey area marks the slowest significant oscillation period found in the data and thus marking a dividing line for whether a peak falls within the “beginning” of the sliding simulation.

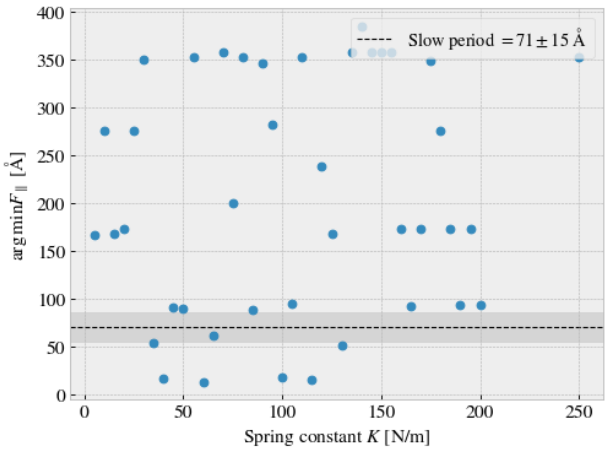


Figure 3.8: Sliding displacement for the max friction peak to appear as a function of spring constant. Fixmove is tmp mapped to $K = 200$ here without any discontinuous lines.

3.4 Out-of-plane buckling

The out-of-plane buckling is one of the original motivations for investigating the application of Kirigami cuts in the context of friction. We perform a stretch simulation in a low temperature $T = 5$ K vacuum in order to verify that we are able to reproduce an out-of-plane buckling with the intended patterns described in Chapter 2. We include the non-cut sheet along with the Tetrahedron (7, 5, 1) and Honeycomb (2, 2, 15) pattern. Despite a visual inspection of the simulation results, using the Open Visualization Tool (OVITO) [SOURCE?](#), we quantify the out-of-plane buckling by assessing the distribution of atoms in the z-direction (perpendicular to the plane) during stretching. We calculate the minimum and maximum z-value taken by the atoms along with the atom count quartiles 1%, 10%, 25%, 50% (median), 75%, 90% and 99% as shown in figure Fig. 3.9. We observe that the Tetrahedron and Honeycomb patterns show a considerable amount of buckling in comparison to the non-cut sheet which exhibit minor buckling of ~ 2 Å which is on the same order as the atomic spacing in the sheet. Furthermore, we notice that the Tetrahedron pattern buckles more in consideration to the min. and max. peaks while the 1% and 99% quartiles is at a similar magnitude as the Honeycomb. By consulting with the simulation visualization this is mainly attributed to fringes on the edge flapping around and thus pushing the min. and max. values.

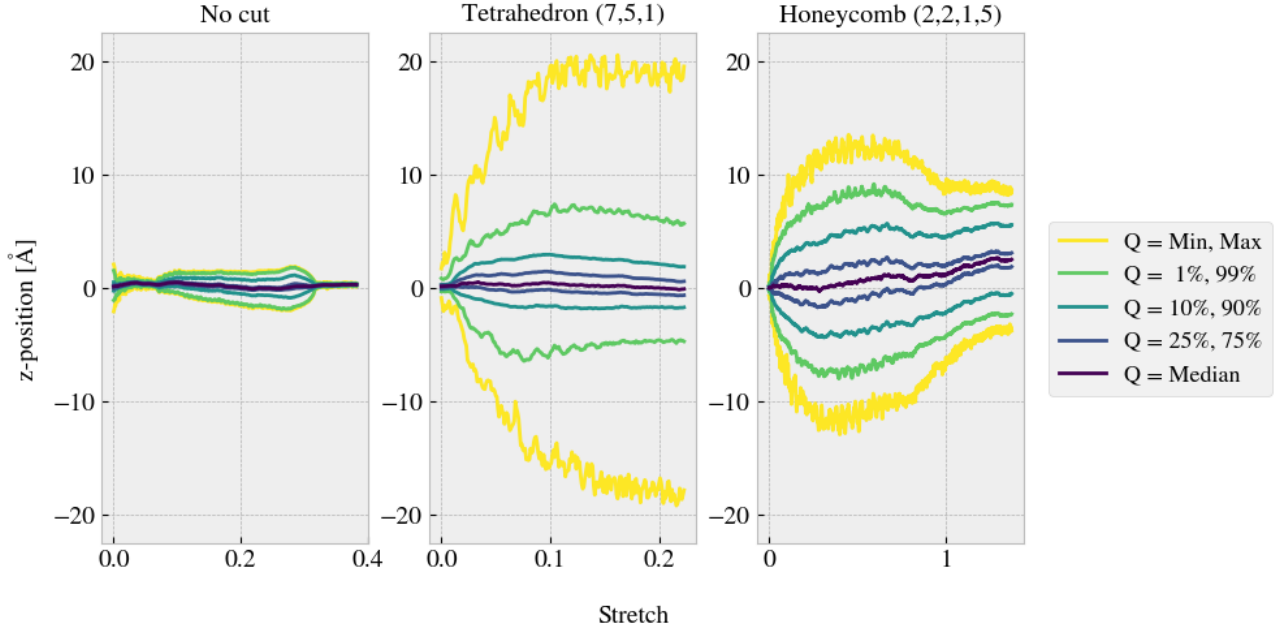


Figure 3.9: Out-of-plane buckling during stretching of the No cut, Tetrahedron (7, 5, 1) and Honeycomb (2, 2, 1, 5) sheet respectively in vacuum at low temperature $T = 5$ K. The buckling is measured by the distribution of the atom z-position (perpendicular to the sheet plane), for which the colors indicates selected quantiles. The yield strain were, reading from left to right, 0.38, 0.22 and 1.37.

The next step is to verify that the buckling will lead to a significant altering of the contact area when the sheet is in put in contact with the substrate. We investigate this by simulating the stretch at the default temperature $T = 300$ K with the presence of contact forces between the sheet and substrate. Note that no normal load is applied as the sheet and substrate is sufficiently attracted by the LJ potential. Selected frames from the simulation is shown in appendix ???. We assess the contact area by the relative amount of atoms in the sheet within chemical range of the substrate. The cut-off for this interaction is 4 Å corresponding to $\sim 120\%$ the LJ equilibrium distance. Since the contact area is usually calculated as the amount of atoms in contact multiplied with an associated area for each contact this feature is taken to be proportional to the contact area. The relative amount of bonds as a function of stretch for the various configurations is shown in figure Fig. 3.10 which clearly indicates a drop in contact area as the cutted sheets are stretched.

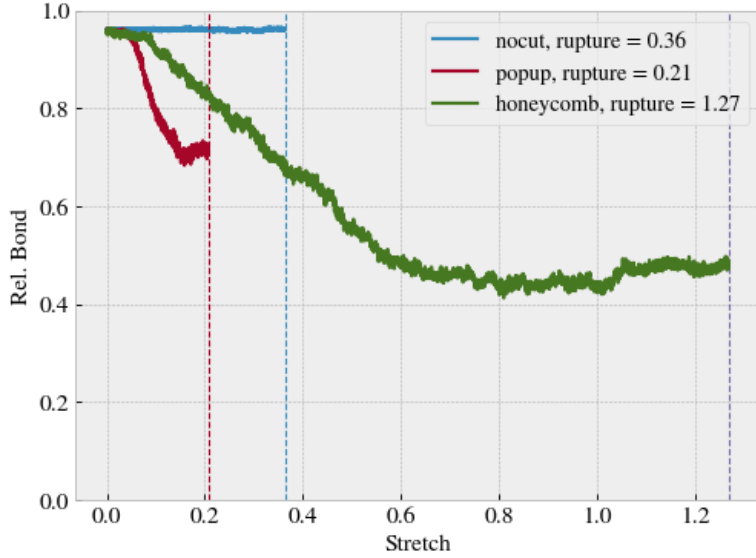


Figure 3.10: Contact vs. stretching of the sheet, where the contact is measured by the relative amount atoms in the sheet within chemical interaction range to the substrate. The cut-off for this interaction range is 4 Å corresponding to $\sim 120\%$ the LJ equilibrium distance. $T = 300$ K

Compare figure Fig. 3.10 to that of figure Fig. 3.15 where multiple simulations constitute the stretch-contact curve.

3.5 Investigating selected parameters

We investigate the importance of the physical variables T , v_{slide} and K (make plots for scan angle as well?) and the choice of timestep dt . This is done partly understand how the dependencies relate to theoretical, numerical and experimental results, and partly to understand how these parameter choices defines the regime for our multi configurational search. We use the default parameters in ?? with exception of the single parameter of interest which is varied in a reasonable range of the default choice. In Fig. 3.11-Fig. 3.14 the kinetic friction estimate and the max friction force is shown as a function of T , v_{slide} , K and dt respectively. For the kinetic friction estimate the absolute error is denoted by a shaded error which linearly connects the points.

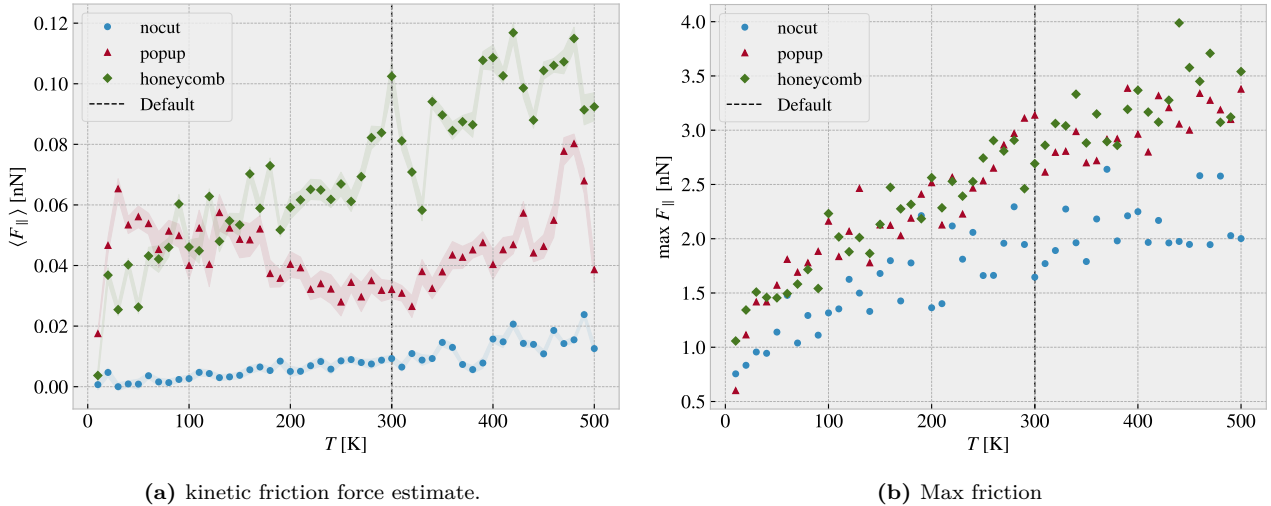


Figure 3.11: Temperature.

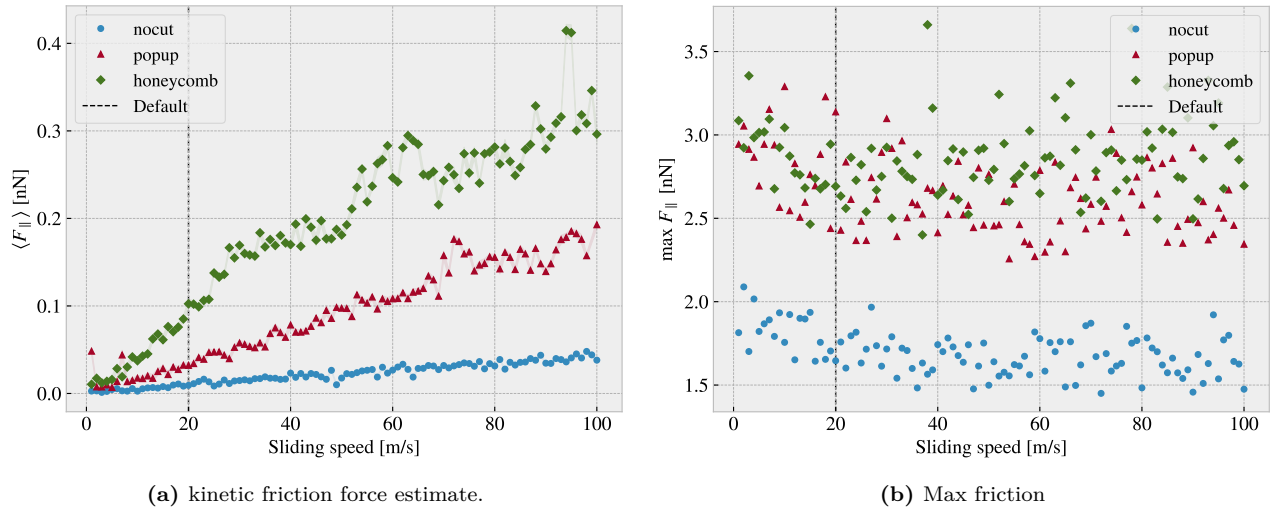


Figure 3.12: Sliding speed

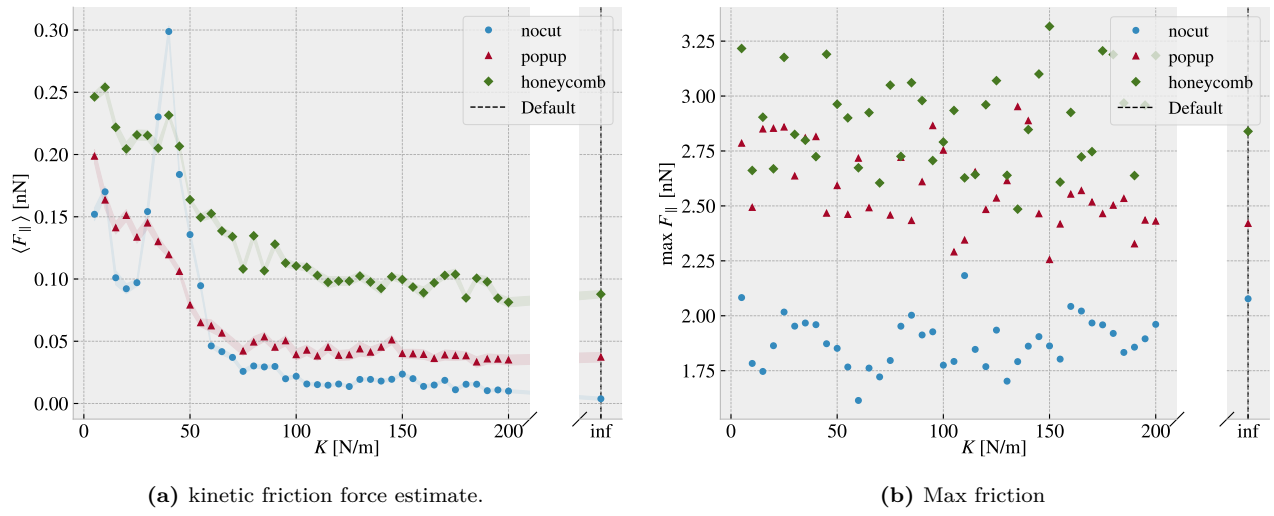


Figure 3.13: Spring constant

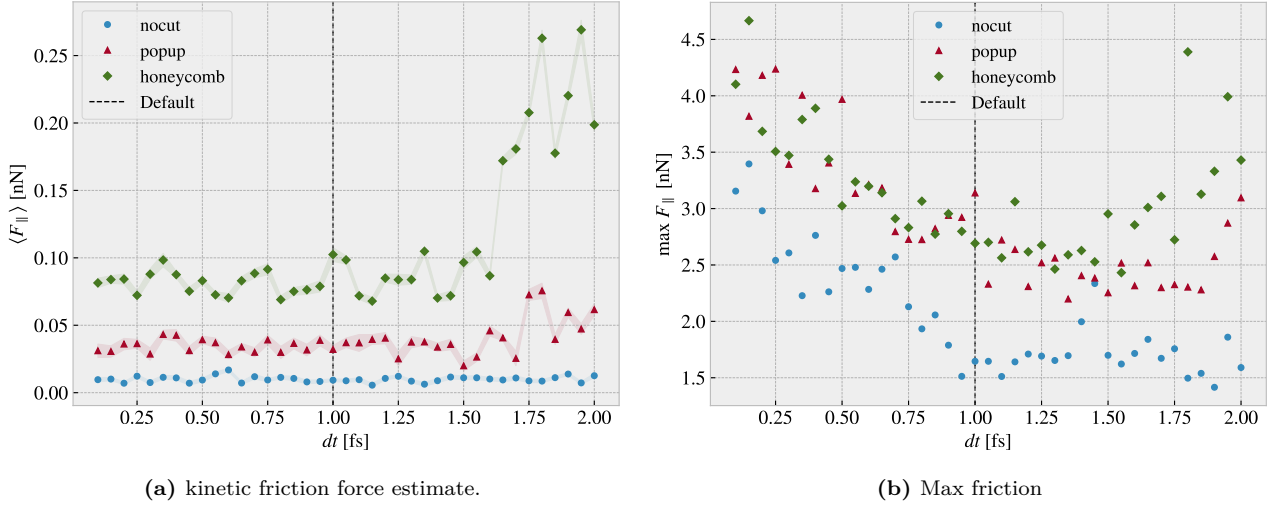


Figure 3.14: Timestep

Quick thoughts:

- Temperature: We do clearly not see the $1/T$ temperature decrease. The non-cut sheet seems to showcase a linear relationship which is also somewhat present for the honeycomb which matches some of the findings in other MD simulations. For the popup we do see a local decrease at low temperatures which flip at around the default $T = 300$ K temperature. The max friction peaks seem to increase with temperature as well indicating that the peaks might be associated with thermal fluctuations rather than actual stick-slip behaviour. This supports the finding that the static friction response is not significantly present in these simulations.
- Velocity: Considering the non-cut sheet first the velocity dependency is seemingly linear which deviates from the expected logarithmic trend. For the cutted configurations we find some peaks which might indicate the presence of resonance frequencies. The cutted sheet might be closer to a logarithmic trend, but this is not spot on either. The max friction seems to decrease slightly with small velocities and then stay rather constant. This can probably be explained by the reduced time to stick between stick slip.
- Spring constant: On all three configurations the kinetic friction decreases with an increasing spring constant. The best explanations might be due to the lack of freedom to “get stuck” in incommensurable configurations. We also notice that the friction varies a lot at lower spring constants supporting the choice of having a stiff spring for stability reasons. Especially the non-cut sheet peaks at $K = 40$ N/m. The max friction seem to be constant with K .
- dt : The kinetic friction is relatively stable around the default choice of $dt = 1$ fs. However, the fluctuations with respect to dt is more significant for popup pattern and even more for the honeycomb pattern. This indicates that the more complex kinetics of the simulation is more sensitive to the timestep. We might interpret this information as an additional measure of uncertainty. The maximum friction decreases with increasing timestep which can be asserted a statistical interpretation: Higher peaks will be captured by the high resolution of a low dt and vice versa. The high max values towards the point of $dt = 2$ fs is most likely due to the approach of instability in the simulation as seen more clearly for the kinetic friction evaluation.

3.6 Normal force and stretch dependencies

Till this point we have only changed variables one by one to investigate single dependencies. We now advance the study to a simultaneous variation of stretch and normal force.

Explain how the stretch is uniformly sampled within equally divided intervals and the normal force is actually uniformly sampled in a given range. Argue that the first might be approximately uniformly distributed for large numbers.

Talk about rupture test also. Maybe in the theory/method section under numerical procedure: Before simulating a rupture test is perform to determine under what stretch the sheet ruptures. This is a slightly higher threshold than when applied normal load and sliding along the substrate.

3.6.1 Pressure reference for normal load domain

In order to relate the magnitude of the normal force in our friction measurement we will use the pressure as a reference. We will use the pressure underneath a stiletto shoe as a worst case for human pressure execution underneath the shoes. From (source 1) it is reported that the diameter of a stiletto heeled shoe can be less than 1 cm. Hence a 80 kg man⁴ standing on one stiletto heel (with all the weight on the heel) will result in a pressure

$$P = \frac{F}{A} = \frac{mg}{r^2\pi} = \frac{80 \text{ kg} \cdot 9.8 \frac{\text{m}}{\text{s}^2}}{(\frac{1 \times 10^{-2} \text{ m}}{2})^2\pi} = 9.98 \text{ MPa}$$

While this is in itself a spectacular realization that is often used in introductory physics courses (source 2) to demonstrate the rather extreme pressure under a stiletto heel (greater than the foot of an elephant) (how many Atmos?) this serves as a reasonable upperbound for human executed pressure. With a full sheet area of $\sim 21 \times 10^3 \text{ \AA}^2$ we can achieve a similar pressure of $\sim 10 \text{ MPa}$ with a normal force of

$$F_N = 10 \text{ MPa} \cdot 21 \times 10^{-17} \text{ m}^2 = 2.10 \text{ nN}$$

Of course this pressure might be insufficient for various industrial purposes, but with no specific procedure in mind this serves as a decent reference point. Notice that if we consider a human foot with area 113 cm^2 the pressure drops to a mere 70 kPa corresponding to $\sim 0.01 \text{ nN}$.

3.6.2 Contact area

??

We reproduce the contact area investigation of Fig. 3.10 with the modification that the contact count is measured as an average of the latter 50% of the sliding simulation at a non-zero applied normal load. The results are shown in Fig. 3.15 with 30 attempted (some rupture) stretch (pseudo) uniformly distributed stretch between 0 and the rupture point and 3 uniform distributed normal loads in the interval [0.1, 10] nN.

⁴Yes, a man can certainly wear stiletto heels.

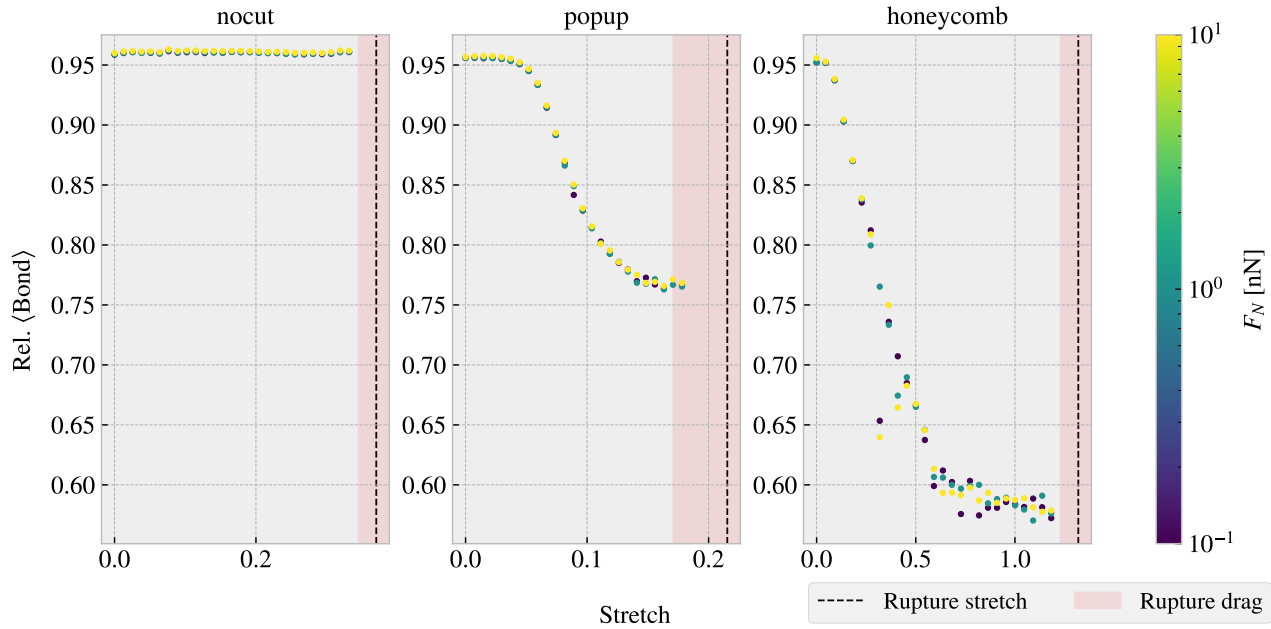


Figure 3.15: Average relative amount of bonds between the sheet and the substrate defined by the cut-off distance of 4 Å. The average is taken over the latter half of the sliding phase. The red shade denotes the stretch range where ruptures accour at certain normal loads under sliding while the black-dotted line represent the rupture point due to stretching (rupture test)

From Fig. 3.10 we observe a significant decrease in the contact due to stretching of the cut configurations in contrast to the non-cut which stays roughly constant. This is reminiscent of the non-sliding stretch vs. contact curve shown in Fig. 3.10. Given these results, theoretically one would expect the kinetic friction to decrease with stretch for the cut configurations.

3.6.3 Stretch

We make a similar analysis as done in the previous section ?? with the substitution of friction force instead of contact (The data is taken from the same simulaitons runs). The kinetic friction force (put uncertainty here even though that it is quite low?) and the max friction is shown in Fig. 3.16a and Fig. 3.16 respectively.

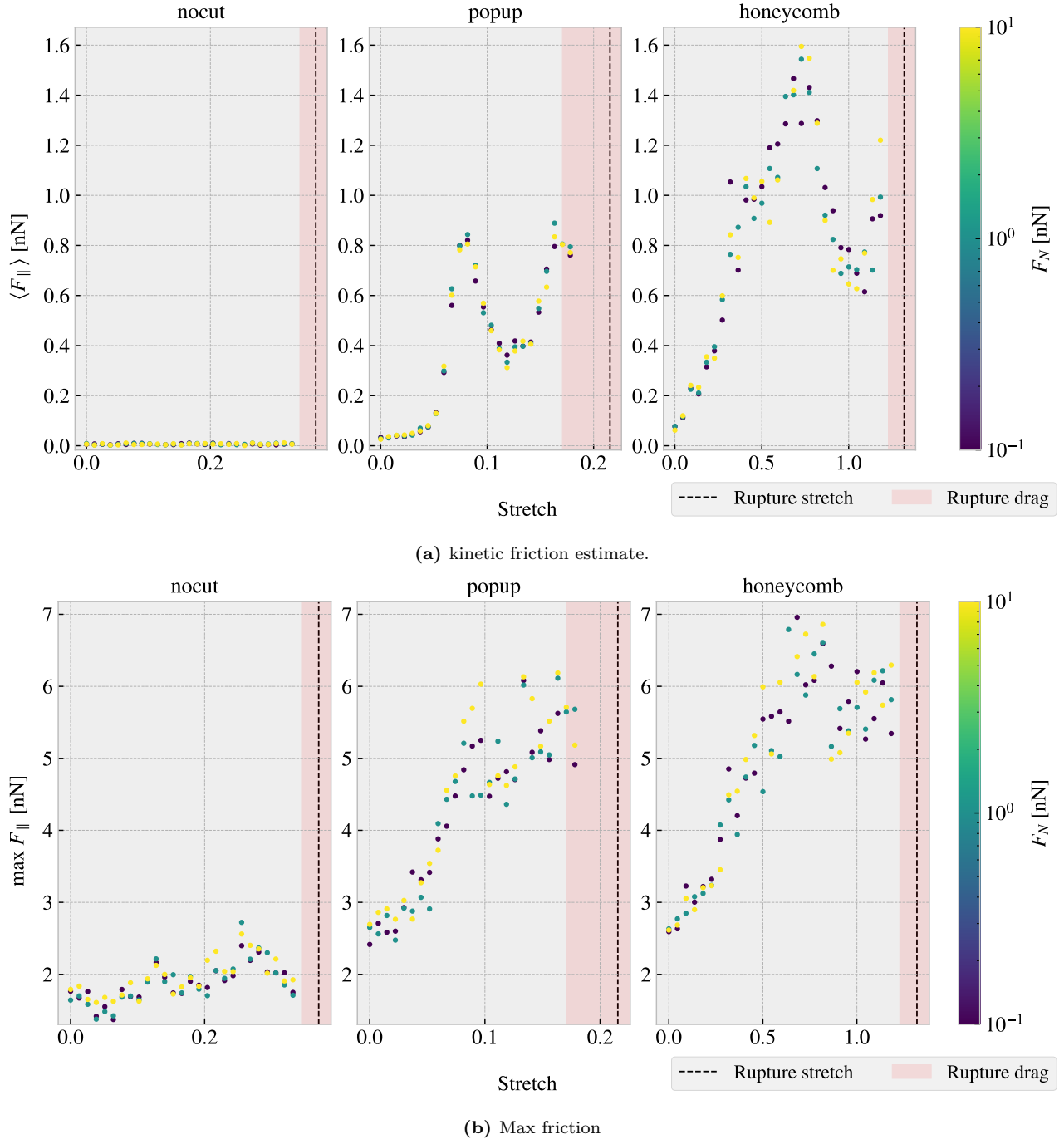


Figure 3.16: CAPTION

From Fig. 3.16a we find to our surprise that the kinetic friction increase with stretch for the cut configurations despite a simultaneous decrease in contact area as shown in figure Fig. 3.15. This suggests that the amount of chemical bonding atoms is not the dominant mechanism for the friction of this system. Instead, we might point to a mechanism more mechanical of nature associated to phonon excitations. When the cut sheet is stretched the stress (show stress maps somewhere or not necessary?) might induce a certain distribution and magnitude of point pressures to favor energy dissipation. Nonetheless, the results showcase a strong coupling between stretch and friction force, also for the max friction force, which is beyond the expectations at this stage of the study. The non-cut configuration does not show significant dependency on the stretch which reveal that this effect is only present when combining cut and stretch and not purely by stretching the sheet.

By considering the increase in kinetic friction towards the first peak we get a relative friction increase and increase vs. stretch ratios as described in Table 3.2. While the honeycomb force increase towards the first peak is approximately linear the popup exhibits seemingly exponential growth which yield a slope on the order ~ 30 nN.

Table 3.2: (stretch, kinetic friction) coordinates from Fig. 3.16a at start and the first peak respectively used to approximate the relative increase in friction force and the ratio for friction increase vs. stretch for sait range. In practice the latter ratio denotes the slope of a forced linear trend.

Configuration	Start	First peak	Relative increase	Friction force vs. stretch ratio [nN]
Popup	$\sim (0, 0.03)$	$\sim (0.082, 0.83)$	27.7	9.76
Honeycomb	$\sim (0, 0.07)$	$\sim (0.728, 1.57)$	22.4	2.06

Additionally, we notice that both the popup and honeycomb also exhibits stretch ranges where the kinetic friction force decrease with increasing stretch. Qualitatively we assign the slope to be on the same order of magnitude as those towards the first peak. This is useful for the prospect of taking advantage of this phenomena as we can essentially achieve both higher and lower friction for increasing stretch for different starting points.

3.6.4 Normal force

Main take away from this section should be that the normal force does not really change the friction much; The friction coefficient is extremely low, but I'm not sure how well the linear fits are (whether they are linear or sublinear). Not sure if I should do a linearly increasing normal force for better linear plots?

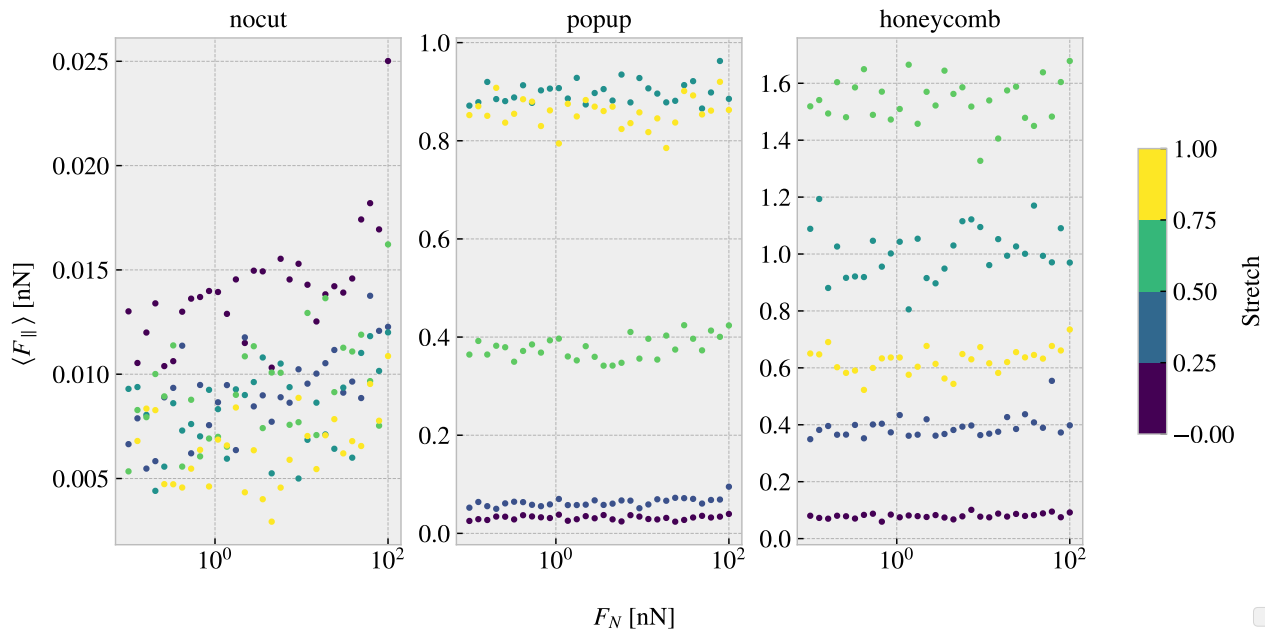


Figure 3.17: ...

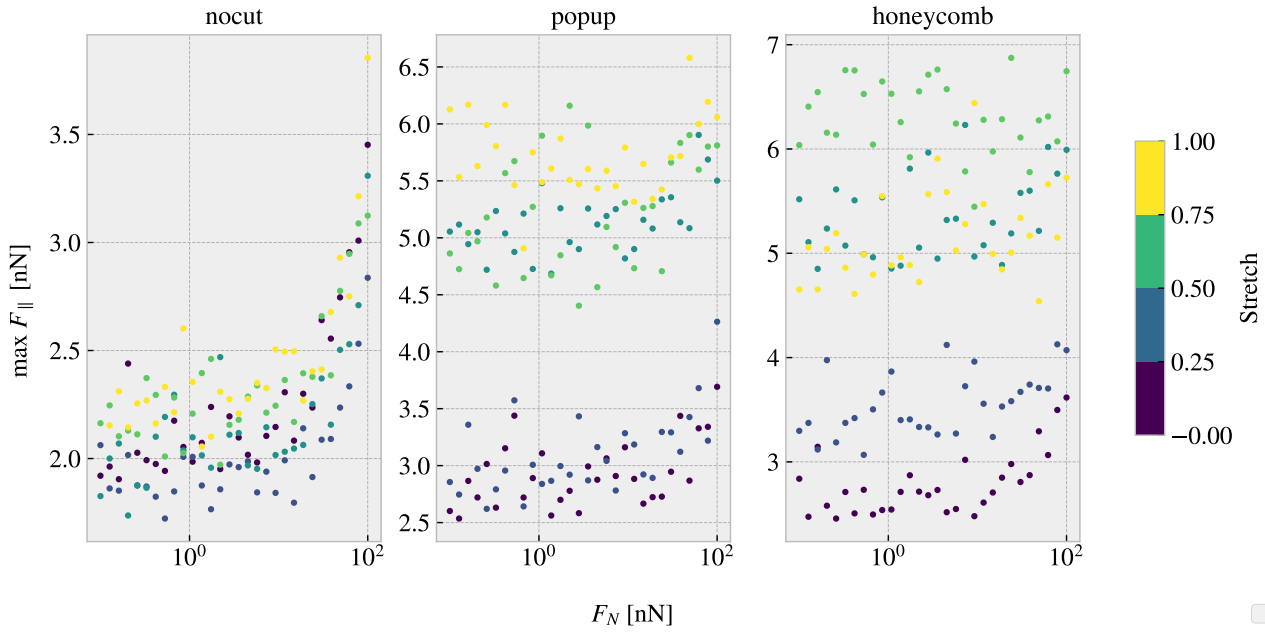


Figure 3.18: Colorbar is only fitted for the right plot (honeycomb)... this should be fixed. Should I have run a linear distribution of FN so I could plot it linear here also...?

Table 3.3: Mean friction coeff

nocut	$0.00009 \pm 1 \times 10^{-5}$	$0.00005 \pm 1 \times 10^{-5}$	$0.00004 \pm 1 \times 10^{-5}$	$0.00005 \pm 2 \times 10^{-5}$	
popup	$0.00005 \pm 3 \times 10^{-5}$	$0.00024 \pm 5 \times 10^{-5}$	$0.0002 \pm 2 \times 10^{-4}$	$0.0005 \pm 1 \times 10^{-4}$	$0.0003 \pm 2 \times 10^{-4}$
honeycomb	$0.00013 \pm 6 \times 10^{-5}$	$0.0006 \pm 3 \times 10^{-4}$	$0.0004 \pm 6 \times 10^{-4}$	$0.0007 \pm 6 \times 10^{-4}$	$0.0009 \pm 3 \times 10^{-4}$

Table 3.4: Max friciton coeff

nocut	$0.0139 \pm 9 \times 10^{-4}$	$0.0083 \pm 7 \times 10^{-4}$	$0.010 \pm 1 \times 10^{-3}$	$0.0105 \pm 9 \times 10^{-4}$	
popup	$0.007 \pm 2 \times 10^{-3}$	$0.010 \pm 2 \times 10^{-3}$	$0.007 \pm 2 \times 10^{-3}$	$0.009 \pm 3 \times 10^{-3}$	$0.006 \pm 2 \times 10^{-3}$
honeycomb	$0.010 \pm 1 \times 10^{-3}$	$0.007 \pm 2 \times 10^{-3}$	$0.007 \pm 3 \times 10^{-3}$	$0.000 \pm 3 \times 10^{-3}$	$0.004 \pm 3 \times 10^{-3}$

One theory for the low friction coefficient might depend on the fact that the normal force is only applied on the pull blocks. Especially with the cut sheet the tension drops such that the effective normal force on the inner sheet is not changing very much. By this theory the friction force vs. normal force on the pull blocks should look a bit more like expected and we might make some plots of those to check

When looking at the graphs for the PB the max friction is visually textbook linear, while the mean friction is a bit more linear but also with negative coefficients...

3.7 Computational cost

Talk about the computational cost of different choices. How does computation time scale with drag speed, dt and maybe T and K as well. One could also mention scaling with system size.

Show how the number of cores per simulation scale to argue that running on just one core (maybe 4) is smart for the next step of many simulations.

Mention the trouble with GPU to show that this was considered, and in fact this was the reason for choosing the Tersoff potential over the AIREBO which is perhaps more common these days...

Appendices

Appendix A

Appendix B

Appendix C

Bibliography

- ¹E. Gnecco and E. Meyer, *Elements of friction theory and nanotribology* (Cambridge University Press, 2015).
- ²Bhusnur, “Introduction”, in *Introduction to tribology* (John Wiley & Sons, Ltd, 2013) Chap. 1, 1–?
- ³H.-J. Kim and D.-E. Kim, “Nano-scale friction: a review”, *International Journal of Precision Engineering and Manufacturing* **10**, 141–151 (2009).
- ⁴K. Holmberg and A. Erdemir, “Influence of tribology on global energy consumption, costs and emissions”, *Friction* **5**, 263–284 (2017).
- ⁵B. Bhushan, “Gecko feet: natural hairy attachment systems for smart adhesion – mechanism, modeling and development of bio-inspired materials”, in *Nanotribology and nanomechanics: an introduction* (Springer Berlin Heidelberg, Berlin, Heidelberg, 2008), pp. 1073–1134.
- ⁶P. Z. Hanakata, E. D. Cubuk, D. K. Campbell, and H. S. Park, “Accelerated search and design of stretchable graphene kirigami using machine learning”, *Phys. Rev. Lett.* **121**, 255304 (2018).
- ⁷P. Z. Hanakata, E. D. Cubuk, D. K. Campbell, and H. S. Park, “Forward and inverse design of kirigami via supervised autoencoder”, *Phys. Rev. Res.* **2**, 042006 (2020).
- ⁸L.-K. Wan, Y.-X. Xue, J.-W. Jiang, and H. S. Park, “Machine learning accelerated search of the strongest graphene/h-bn interface with designed fracture properties”, *Journal of Applied Physics* **133**, 024302 (2023).
- ⁹Y. Mao, Q. He, and X. Zhao, “Designing complex architectured materials with generative adversarial networks”, *Science Advances* **6**, eaaz4169 (2020).
- ¹⁰Z. Yang, C.-H. Yu, and M. J. Buehler, “Deep learning model to predict complex stress and strain fields in hierarchical composites”, *Science Advances* **7**, eabd7416 (2021).
- ¹¹A. E. Forte, P. Z. Hanakata, L. Jin, E. Zari, A. Zareei, M. C. Fernandes, L. Sumner, J. Alvarez, and K. Bertoldi, “Inverse design of inflatable soft membranes through machine learning”, *Advanced Functional Materials* **32**, 2111610 (2022).
- ¹²S. Chen, J. Chen, X. Zhang, Z.-Y. Li, and J. Li, “Kirigami/origami: unfolding the new regime of advanced 3D microfabrication/nanofabrication with “folding””, *Light: Science & Applications* **9**, 75 (2020).
- ¹³Z. Deng, A. Smolyanitsky, Q. Li, X.-Q. Feng, and R. J. Cannara, “Adhesion-dependent negative friction coefficient on chemically modified graphite at the nanoscale”, *Nature Materials* **11**, 1032–1037 (2012).
- ¹⁴R. W. Liefferink, B. Weber, C. Coulais, and D. Bonn, “Geometric control of sliding friction”, *Extreme Mechanics Letters* **49**, 101475 (2021).
- ¹⁵L. Burrows, *New pop-up strategy inspired by cuts, not folds*, (Feb. 24, 2017) <https://seas.harvard.edu/news/2017/02/new-pop-strategy-inspired-cuts-not-folds>.
- ¹⁶Scotch cushion lock protective wrap, https://www.scotchbrand.com/3M/en_US/scotch-brand/products/catalog/~/Scotch-Cushion-Lock-Protective-Wrap/?N=4335+3288092498+3294529207&rtr=rud.
- ¹⁷P. Zhu and R. Li, “Study of nanoscale friction behaviors of graphene on gold substrates using molecular dynamics”, *Nanoscale Research Letters* **13**, 34 (2018).